

Unifying the design space of truss metamaterials by generative modeling

Li Zheng¹, Siddhant Kumar^{2,*}, and Dennis M. Kochmann^{1,*}

¹Mechanics & Materials Lab, Department of Mechanical and Process Engineering, ETH Zürich, 8092 Zürich, Switzerland

²Department of Materials Science and Engineering, Delft University of Technology, 2628 CD Delft, Netherlands

*sid.kumar@tudelft.nl, dmk@ethz.ch

ABSTRACT

The rise of machine learning has fueled the discovery of new materials and, especially, metamaterials—truss lattices being their most prominent class. While their tailorable properties have been explored extensively, the design of truss-based metamaterials has remained highly limited and often heuristic, due to the vast, discrete design space and the lack of a comprehensive parameterization. We here present a graph-based deep learning generative framework, which combines a variational autoencoder and a property predictor, to construct a reduced, continuous latent representation covering an enormous range of trusses. This unified latent space allows for the fast generation of new designs through simple operations (e.g., traversing the latent space or interpolating between structures). We further demonstrate an optimization framework for the inverse design of trusses with customized properties, including exceptionally stiff, auxetic, and pentamode-like designs. This generative model can predict manufacturable (and counter-intuitive) designs with extreme target properties beyond the training domain.

Introduction

Architected metamaterials are rapidly redefining the boundaries of achievable material properties. Supported by additive manufacturing, the design of such cellular solids with tailored microstructural architecture has led to unprecedented functionality: from counter-intuitive negative compressibility^{1,2} and negative Poisson’s ratio^{3,4} to mechanical cloaking⁵, extreme energy absorption^{6–8}, and guided acoustic waves^{9,10}. Among the myriad of available design spaces, truss metamaterials – based on periodic lattices of beam networks – have emerged as the dominant one, particularly due to their high stiffness and strength in the ultralow-relative-density regime^{11–16} and the simple manufacturability.

Truss metamaterials offer an extensively tunable design space based on both the lattice topology (i.e., the connectivity of the beam network) as well as geometric features (e.g., the length, orientation, and cross-sectional shape of each strut). However, most of this unlimited design freedom has remained untapped. Many design applications^{17–21} have been limited to a small catalog of ad-hoc lattices (e.g., kagome, octet, and octahedron^{22–28}), which have been identified through a combination of intuition and trial-and-error over the years. While the catalog-based search space can be enriched by tuning geometric features²⁹ or base material properties¹⁹, it is strongly limited in topological tunability and fails to exploit the full range of achievable designs and hence of achievable effective metamaterial properties. Many truss optimization solutions have adopted heuristic search strategies to find optimal structures by iteratively adjusting the active beams and/or nodes in the design domain, according to mechanics-based criteria^{30–33}. This, however, becomes computationally infeasible in large-scale problems due to the enormous and noisy search space. Recently, Lumpe and Stankovic³⁴ proposed an extensive catalog of truss lattices by mimicking the molecular structure of crystalline lattices. Yet, the same fundamental issue persists as for all such catalogs of truss lattices with different topologies: there exists no finite-dimensional, continuous, and seamless design space. For example, while the “kagome” vs. “octet” lattice is interpretable by humans, it is not directly cognizant to a computer. The question is hence: how does one translate distinct lattice topologies into a unified, finite-dimensional, vector-based parameterization that can be understood by an algorithm aiming to optimize the lattice design for certain target metamaterial properties? While a pixelated/voxelated image-based parameterization (similar to conventional topology optimization) is a solution in principle, capturing slender beams in truss lattices warrants extremely high resolution,

which again becomes prohibitively expensive.

To address the aforementioned limitations, we introduce a graph-theoretic approach to represent a vast design space of three-dimensional (3D) truss topologies. Every truss lattice can be naturally translated into a graph – a mathematical structure consisting of edges and nodes (i.e., struts and their intersections, respectively). The edges encode the lattice topology in the form of a nodal adjacency matrix; the nodes encode the geometric features in the form of spatial coordinates. Additional graph-level information may include, e.g., strut thickness or further cross-sectional information. While a graph as a data structure is computationally interpretable, the discontinuities across different lattice topologies are also persistent in the graph representation.

We introduce a machine learning (ML) framework to extract a generalizable and unified design space for truss lattices with diverse topologies. ML has made a significant impact in the design of metamaterials – from data-driven surrogate models for accelerating multiscale simulations^{35–40} to the inverse design for tailored properties^{41–47}. Of particular interest to our context are generative ML models (using, e.g., variational autoencoders⁴⁸ (VAEs) and generative adversarial networks⁴⁹ (GANs)), which aim to learn the underlying distribution of the data itself (as opposed to discriminative models that learn to predict labels for a given input) and have been used to successfully design metamaterials^{21,50–52}. However, unlike in those approaches where the design parameterization can be formulated as a finite-dimensional vector or image, we turn to the special class of generative graph-based ML models for dealing with graph representations of truss lattices. Graph-based learning has recently gained prominence because of its ability to model non-Euclidean data representing interrelations in irregular domains, such as social networks,^{53–55} chemical molecules,^{56,57} and material microstructures^{37,58}. Distinct from existing works that utilize supervised graph-based models as surrogate models to provide real-time prediction of various properties of interest, e.g., homogenized elastic⁵⁹ and thermal properties⁶⁰ or dominant deformation mechanism⁶¹ of lattice architectures, the goal of the graph generative modeling framework proposed here is to construct a unified, continuous latent representation of a vast and discrete truss design space and its exploitation for the inverse design for targeted mechanical properties. We here demonstrate that a VAE can successfully abstract a hidden or latent design representation of diverse graph-based truss lattices. This is achieved by using a neural network architecture, which contains an informational bottleneck and enables compressing the high-dimensional graph representation into a finite, low-dimensional, and smooth vector representation. In this latent space, any two lattices with similar topological and geometric features are located close to each other, whereas any two distant lattices can be continuously transformed into each other. New lattice designs can be straightforwardly generated by randomly sampling in the latent space. Exploration of this latent space further allows us to seamlessly search or optimize for truss lattices with exotic or tailored properties – including those that lie outside the domain of the available training data.

Results

Creating the design space

We begin by introducing our definition of the design space of truss lattices. From a practical standpoint, we focus our attention on lattices based on the periodic tessellation of a cubic representative volume element (RVE). Inspired by the cube decomposition approach⁶², we partition the RVE into eight equal cubes, the octants, as shown in Figure 1a. By assuming symmetries across the three mutually orthogonal symmetry planes, it is sufficient to define the truss only within a single octant, which simplifies the complex optimization problem while ensuring great flexibility and periodic tilability. Following the graph representation of molecules^{59,63}, truss-like structures can be described by a set of nodes connected by solid beams, which form the nodes and edges of the graph, respectively. To create a sufficiently large design space of truss structures, we define a total of 27 possible node placements within the octant (Figure 1a): 8 vertex nodes $\{v_0, v_1, v_2, v_3, v_4, v_5, v_6, v_7\}$, 12 edge nodes $\{e_0, e_1, e_2, e_3, e_4, e_5, e_6, e_7, e_8, e_9, e_{10}, e_{11}\}$, 6 face nodes $\{f_0, f_1, f_2, f_3, f_4, f_5\}$, and a single body node $\{t_0\}$ within the volume. While the body node is free to move in 3D, edge and face nodes are restricted to be displaced only along the edge and within the face, respectively, and vertex nodes are fixed, as illustrated in Figure 1a. We define the offsets of nodes (as in ref.⁶²) in the natural coordinate system, representing their relative positions with respect to the fixed vertex nodes to ensure connectivity on the outer boundaries. The complete set of *node features* \mathbf{x} contains the offset of each node in its movable direction(s).

Analogous to the above node features, the *structural features* of the unit cell include the truss topology, which is fully described by a list of all edges (e.g., (e_0, f_1) represents a beam connecting edge node e_0 and face node f_1). By analogy with a graph structure, we represent the lattice topology using an *adjacency matrix* $\mathbf{A} \in \{0, 1\}^{n \times n}$, where the diagonal elements $A_{ii} = 1$ (for all $i = 1, \dots, n$) and $n = 27$ is the total number of nodes. The adjacency matrix

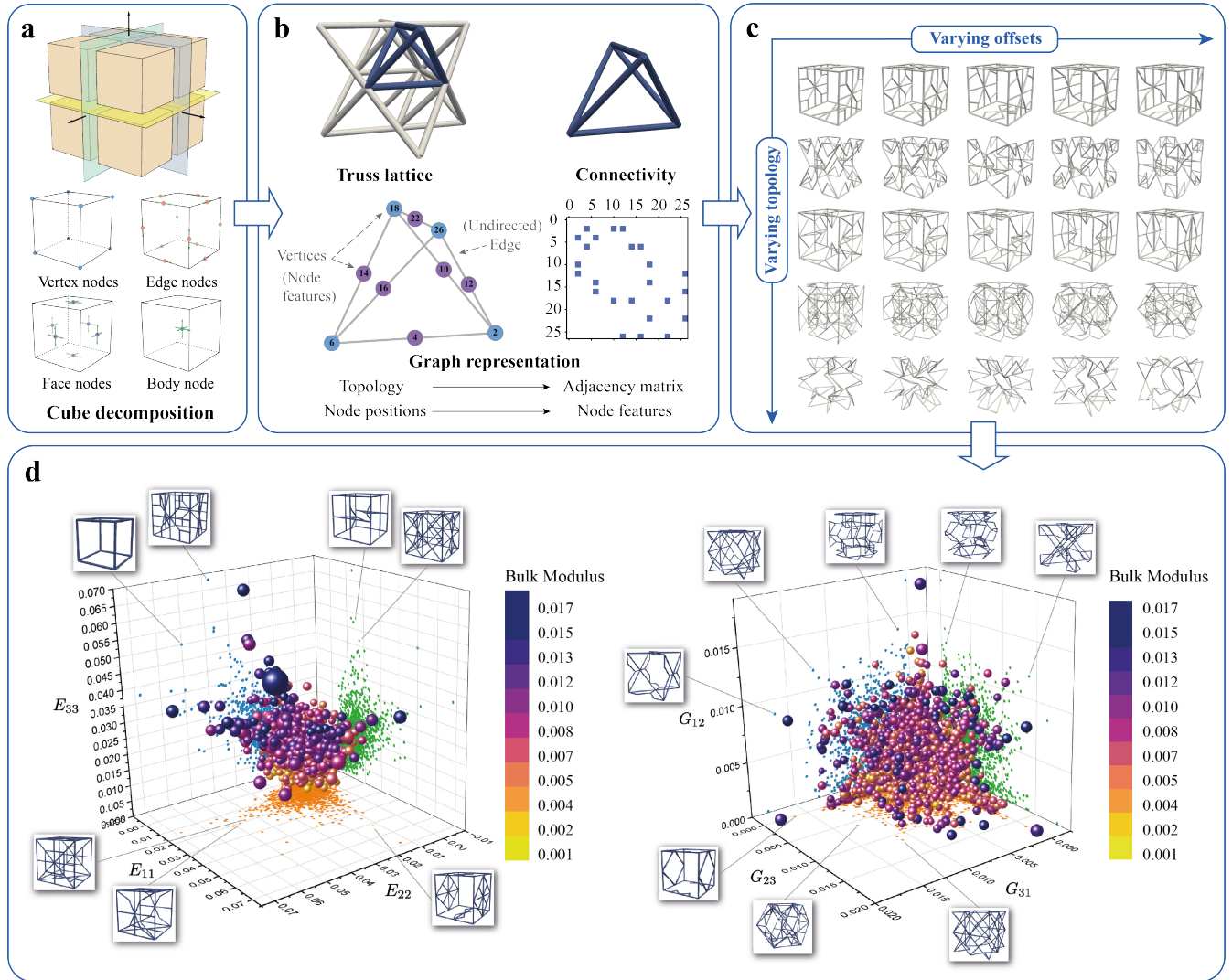


Figure 1. Overview of the truss parametrization and the data generation scheme used to create a diverse truss lattice dataset. (a) Cube decomposition generates the irreducible truss pattern with possible node placements and the nodes' degrees of freedom defined on the octant. For example, an edge node has one degree of freedom and is only allowed to traverse along the edge, while a face node with two degrees of freedom can assume at any position within the plane. (b) Graph representation of an octet truss example, whose vertices and beams serve as input to the VAE model. The lattice is defined by the adjacency matrix and node features. (c) Examples of different truss lattices are realized by varying the topology and the vertex degrees of freedom as well as the strut diameters, showcasing the wide coverage of the design space. (d) Effective directional Young's moduli E and effective shear moduli G (normalized by the respective properties E_s and G_s of the base material) and their projected values of 3,000 structures randomly drawn from the dataset, and selected examples with extreme properties. The size of the markers is proportional to the strut radius of the unit cell; their colors indicate the effective bulk modulus. The effective stiffness was obtained by finite element (FE) homogenization with periodic boundary conditions; the radius of circular cylindrical struts is scaled to maintain a constant relative density of $\rho = 0.15$. The resulting variety of truss configurations in the dataset covers a large range of elastic properties.

serves as a lookup table, where the value of 1 denotes an edge between nodes, whereas 0 indicates that an edge is not present. With the graph representation, introducing or removing beams from the truss can be easily achieved by operations on the adjacency matrix (e.g., the superposition of two structures is described by the logical disjunction, i.e., element-wise boolean OR, of two adjacency matrices). Possible defects, such as isolated nodes or struts, can be efficiently identified and resolved by examining the adjacency matrix. Here we do not explicitly consider permutation invariance or equivariance of graphs due to the inherent representation complexity in generative modeling tasks^{64,65}. In other scenarios (such as predicting frame-indifferent properties^{37,66}), incorporating permutation invariance or symmetry groups such as SE(3) in graph representations^{67–70} could largely enhance the learning of the underlying relations of various structural configurations.

We leverage the above representation to construct a dataset containing a large family of truss lattices covering a wide range of mechanical properties. To this end, we begin with a set of three well-known elementary trusses as initial topologies, including the octet, body-centered-cubic, and simple cubic unit cells as $1 \times 1 \times 1$ and $2 \times 2 \times 2$ tessellations. Starting from those, an iterative stochastic perturbation algorithm generates novel structures by randomly inserting/removing both nodes (of edge, vertex, face, or body types) and truss connectivities. New connections are created by connecting newly inserted nodes to at least one of their nearest neighbor nodes. Random perturbations are added to the position of all nodes, while obeying the corresponding positional constraints of the vertex, edge, and face nodes. The above procedure is repeated until the obtained truss lattice satisfies the constraints on the graph connectivity (details provided in Supplementary Note 1). We build a large preliminary library, which includes a variety of trusses – from well-studied structures to unconventional ones, as shown in Figure 1c. From the thus-obtained preliminary library, new lattices are created by superimposing two randomly sampled structures (with repetitions allowed). To ensure the physical feasibility of structures generated by random perturbations and superpositions, we enforce the constraint that the lattice is self-connected; i.e., the truss graph must have exactly one maximally connected subgraph spanning the whole graph. Intersecting beams, which may arise from the superposition of different topologies, are fixed by splitting the involved beams and inserting a new node at the intersection point. The resulting lattices constitute the design space as well as the corresponding dataset for machine learning.

By perturbing both the topological and geometrical features of the lattice, we create a rich database of anisotropic lattices, consisting of 965,736 unique structures. As a representative and important mechanical property, we study the full anisotropic 3D elastic stiffness tensor. All lattices obtained from the cube decomposition approach naturally possess three orthogonal plane reflection symmetries and therefore only require nine independent components to describe the orthotropic homogenized stiffness tensor; we select $\mathbf{S} = (\mathbb{C}_{1111}, \mathbb{C}_{1122}, \mathbb{C}_{1133}, \mathbb{C}_{2222}, \mathbb{C}_{2233}, \mathbb{C}_{3333}, \mathbb{C}_{2323}, \mathbb{C}_{3131}, \mathbb{C}_{1212})$. For each structure, the effective mechanical stiffness tensor is computed by homogenization, using a finite element (FE) framework, which models individual struts as linear elastic Timoshenko beams with a circular cross-section⁷¹. We assume a homogeneous base material with Poisson’s ratio $\nu_s = 0.3$ and unit Young’s modulus $E_s = 1$ (i.e., all reported effective stiffness values are relative to the base material’s Young’s modulus). The beam thickness d of all struts is varied such that a constant relative density $\rho = 0.15$ is maintained across all structures. This will be helpful during property optimization, as it ensures that optimized mechanical properties do not come at the cost of an increased weight.

To visualize the property range reached by the established truss catalog, Figure 1d shows the effective directional Young’s moduli E and the effective shear moduli G along the three principle cubic directions and their projections onto the x - y -, x - z -, and y - z -planes. Results show that the established truss database covers a wide range of Young’s moduli, spanning three orders of magnitude between 10^{-5} and 10^{-2} times the base material’s Young’s modulus. Although the initial structures used as seeds are limited to cubic symmetry, the resulting library generated by perturbing both the truss connectivity and node positions exhibits strong anisotropy and has significantly expanded the range of mechanical properties (e.g., the representative examples shown in Figure 1d reach effective Young’s moduli E_{33} of ca. 36% higher than that of a simple cubic unit cell in the principle direction at the same density). Of course, the dataset could be enriched by more unique structures, using the above approach. Yet, we limit our study to the current dataset based on the performance and computational cost of the machine learning model (as detailed below). The data generation could also be generalized to other truss families. For example, while we only consider centrosymmetric unit cells, non-centrosymmetric unit cells can be readily constructed in a similar manner by allowing for different structures in each octant instead of applying symmetries. Compared to prior approaches that have focused on a truss unit cell catalog, our database achieves a significantly wider design space of truss structures with a relatively compact formulation based on graphs.

Generative modeling framework

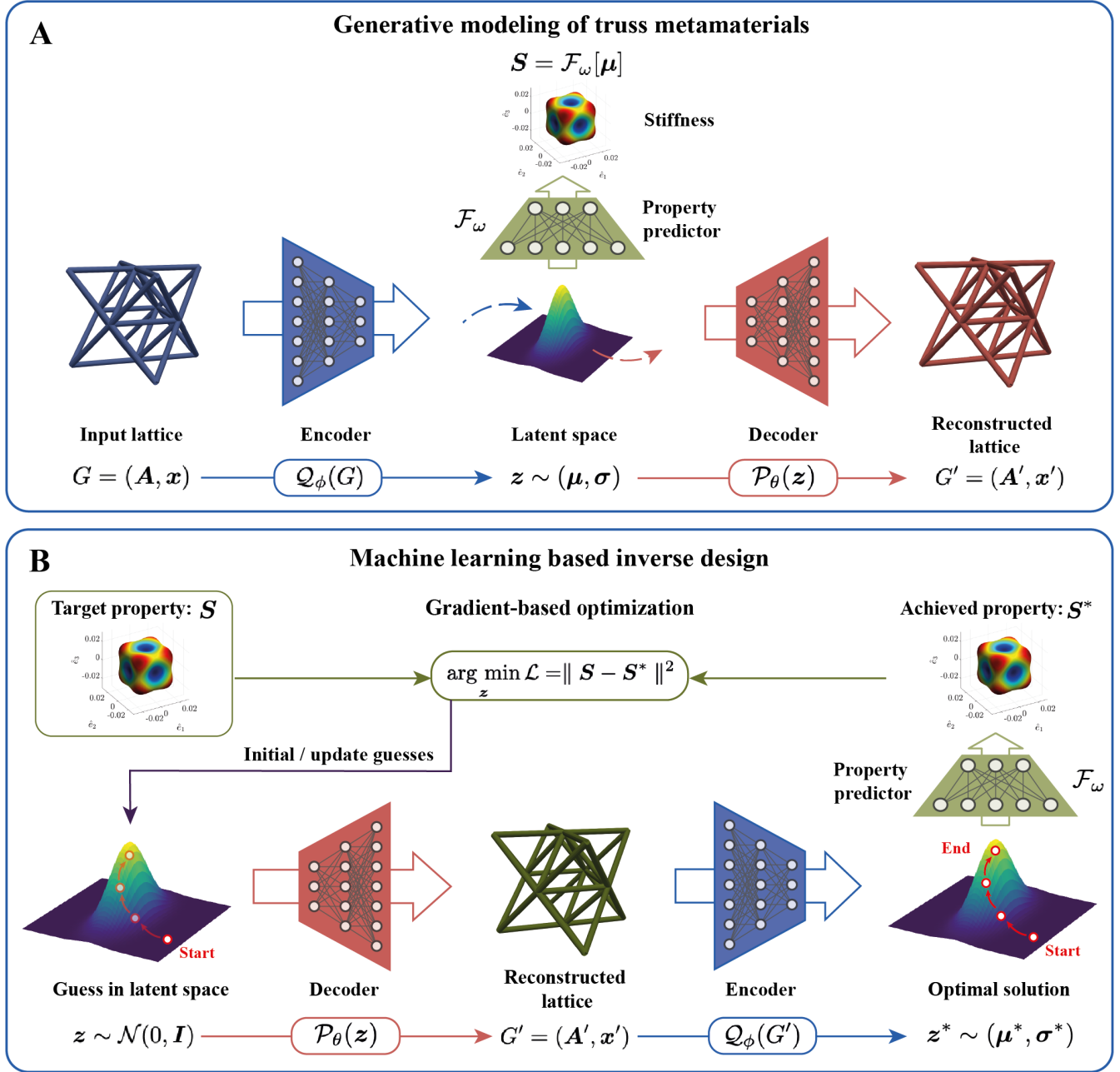


Figure 2. Generative modeling framework. (a) The VAE model takes the graph representation $G = (\mathbf{A}, \mathbf{x})$ of truss lattices as input and learns a continuous latent space over the geometries of various trusses. The reduced representation \mathbf{z} of truss structures is then passed to the decoder to reconstruct the lattice. An augmented MLP neural network predicts the mechanical properties of trusses based on their latent representation \mathbf{z} . (b) The inverse design framework aims to generate truss lattices with target properties. Starting with the 100 closest matches in the training dataset as initial guesses, gradient-based optimization is applied to search for possible lattices with desirable properties. The inverse design candidate structures are passed to the encoder to obtain their corresponding latent representations, which are then forwarded to the property predictor to predict the effective stiffness of the proposed lattices.

The proposed design space for truss lattices is discrete and discontinuous. For example, any two truss lattices may have different numbers of nodes or nodes with different numbers of degrees of freedom (such as edge vs. face nodes). However, representing the truss lattices by a graph structure, as described above, enables the use of node features and adjacency matrix as inputs for a machine learning model to learn a low-dimensional, continuous and smooth

representation for the high-dimensional, discrete, and intractable graph representation.

We use a VAE containing two neural networks – an *encoder* and a *decoder* (see Figure 2a for a schematic of the framework). Let $G = (\mathbf{A}, \mathbf{x})$ denote the graph representation of a truss lattice, defined by its adjacency matrix and node features. The encoder \mathcal{Q}_ϕ (with the set of trainable parameters ϕ) maps an input graph G into two d -dimensional vectors $\boldsymbol{\mu}(G; \phi) \in \mathbb{R}^d$ and $\boldsymbol{\sigma}(G; \phi) \in \mathbb{R}^d$, which respectively prescribe the mean and covariance of a diagonal multivariate Gaussian distribution

$$\mathbf{z} \sim \mathcal{N}([\mu_1, \dots, \mu_d]^\top, \text{diag}([\sigma_1^2, \dots, \sigma_d^2]^\top)). \quad (1)$$

Here, $\mathbf{z} \in \mathbb{R}^d$ denotes a low-dimensional vector encoding of the input graph G , also known as latent representation. While the formulation is presented in terms of $\boldsymbol{\sigma}$, the neural network predicts $\log \boldsymbol{\sigma}$. To maintain differentiability (required for backpropagation-based neural network training), \mathbf{z} is sampled using the reparameterization trick⁴⁸ as

$$\mathbf{z} = \boldsymbol{\mu} + \boldsymbol{\varepsilon} \odot [\sigma_1, \dots, \sigma_d]^\top \quad \text{with} \quad \boldsymbol{\varepsilon} \sim \mathcal{N}(\mathbf{0}, \mathbf{I}), \quad (2)$$

where \odot denotes element-wise multiplication. The decoder \mathcal{P}_θ (with set of trainable parameters θ) maps the latent vector \mathbf{z} into a graph representation $G' = (\mathbf{A}', \mathbf{x}') = \mathcal{P}_\theta(\mathbf{z}; \theta)$ and attempts to accurately reconstruct the original graph, i.e., $G \approx G'$. The autoencoding of the input graphs with such a neural network structure creates an information bottleneck⁷² in the latent representation. The information bottleneck only preserves the necessary meaningful information to allow accurate reconstruction of the graphs, with a significant reduction in the dimension and complexity of the original data. Consequently, in the latent space any two graphs/lattices with similar topology and geometry are located close to each other; any two distant graphs/lattices can be continuously transformed between each other by traversing the latent space.

We here adopt the attributed network embedding method⁷³ to learn the individual dependencies of the structural topology and node placements as well as their combined effects (details provided in Supplementary Note 3.2). Specifically, the adjacency matrix (containing binary values) and node features (containing continuous values) are serialized and passed through separate encoders to obtain the respective latent space distribution means $\boldsymbol{\mu}^A \in \mathbb{R}^{d_A}$ and $\boldsymbol{\mu}^x \in \mathbb{R}^{d_x}$ and standard deviations $\boldsymbol{\sigma}^A \in \mathbb{R}^{d_A}$ and $\boldsymbol{\sigma}^x \in \mathbb{R}^{d_x}$. The embedding dimensions d_A and d_x are chosen such that $d_{Ax} = (d_A + d_x) - d > 0$. Note that, since the adjacency matrix is symmetric, only the upper triangular part is considered by the encoder. The final latent space distribution is obtained by partial overlap of the adjacency matrix and node features embeddings. The mean is given by

$$\boldsymbol{\mu} = \underbrace{\begin{bmatrix} \mu_1^A \\ \vdots \\ \mu_{d_A - d_{Ax}}^A \end{bmatrix}}_{\text{topology-specific}} \oplus \frac{1}{2} \left(\underbrace{\begin{bmatrix} \mu_{d_A - d_{Ax} + 1}^A \\ \vdots \\ \mu_{d_A}^A \end{bmatrix} + \begin{bmatrix} \mu_1^x \\ \vdots \\ \mu_{d_{Ax}}^x \end{bmatrix}}_{\text{shared topology and geometry}} \right) \oplus \underbrace{\begin{bmatrix} \mu_{d_{Ax} + 1}^x \\ \vdots \\ \mu_{d_x}^x \end{bmatrix}}_{\text{geometry-specific}}, \quad (3)$$

where \oplus denotes vector concatenation (the logarithm of the standard deviation, i.e., $\log \boldsymbol{\sigma}$, is obtained analogously using $\log \boldsymbol{\sigma}^A$ and $\log \boldsymbol{\sigma}^x$). Since the adjacency matrix and node features influence the topology and geometry, respectively, subsets of the latent space dimensions offer topology-specific, geometry-specific, and shared control over the design space, the advantages of which will become apparent when discussing the results. Similar to the encoding, two separate decoders are used to output the graph $G' = (\mathbf{A}', \mathbf{x}')$ from a latent vector \mathbf{z} – the topology-specific and shared dimensions of \mathbf{z} are used to obtain the adjacency matrix \mathbf{A}' ; the shared and geometry-specific dimensions of \mathbf{z} are used to obtain the node features \mathbf{x}' .

Towards the efficient data-driven design and the discovery of new structures with desirable properties, the latent space can be associated with specific properties that we seek to optimize by a neural network surrogate model using the latent vectors as input, thus bypassing the costly FE homogenization computation. Therefore, we adapt the original VAE structure and link the latent space to the homogenized effective stiffness measures \mathbf{S} by feeding the mean of the latent vector, i.e., $\boldsymbol{\mu}(G; \phi)$, into an additional neural-network-based property predictor \mathcal{F}_ω (with trainable parameters ω).

Given a representative dataset $\mathcal{D} = \{(G^{(n)}, \mathbf{S}^{(n)}) : n = 1, \dots, N\}$ containing N structure-property pairs, the VAE

and property predictor are jointly trained as

$$\begin{aligned}
\theta, \phi, \omega \leftarrow \arg \min_{\theta, \phi, \omega} & \underbrace{\frac{1}{N} \sum_{n=1}^N \left(\left\| \mathbf{A}^{(n)} - \mathbf{A}^{(n)'} \right\|^2 + \left\| \mathbf{x}^{(n)} - \mathbf{x}^{(n)'} \right\|^2 \right)}_{\text{reconstruction loss}} + \underbrace{\frac{1}{N} \sum_{n=1}^N \left\| \mathbf{S}^{(n)} - \mathcal{F}_\omega[\boldsymbol{\mu}^{(n)}] \right\|^2}_{\text{property prediction loss}} \\
& + \underbrace{\sum_{n=1}^N D_{\text{KL}} \left(\mathcal{N} \left(\left[\mu_1^{(n)}, \dots, \mu_d^{(n)} \right]^\top, \text{diag} \left(\left[\sigma_1^{(n)2}, \dots, \sigma_d^{(n)2} \right]^\top \right) \right) \parallel \mathcal{N}(\mathbf{0}, \mathbf{I}) \right)}_{\text{Kullback-Leibler divergence}}.
\end{aligned} \tag{4}$$

The *reconstruction loss* enforces that the encoded graphs (equivalently, truss lattices) are accurately reconstructed (in terms of both the adjacency matrix and node features) by the decoder. The *property prediction loss* enforces that the property predictor outputs the stiffness of a truss lattice accurately. The Kullback–Leibler divergence (KLD)⁴⁸ penalizes the divergence of the probability distribution of the latent space produced by the encoder from the standard Gaussian distribution $\mathcal{N}(\mathbf{0}, \mathbf{I})$. This allows directly sampling the latent space using a standard Gaussian distribution and decoding truss lattices during the inference stage (as opposed to first encoding an a-priori known lattice into a latent vector and then decoding back during training), which in turn enables the design and discovery of novel trusses beyond the dataset at hand. The KLD loss further simplifies to

$$D_{\text{KL}} \left(\mathcal{N} \left([\mu_1, \dots, \mu_d]^\top, \text{diag} \left([\sigma_1^2, \dots, \sigma_d^2]^\top \right) \right) \parallel \mathcal{N}(\mathbf{0}, \mathbf{I}) \right) = \frac{1}{2} \sum_{j=1}^d [\sigma_j^2 + \mu_j^2 - 1 - \log(\sigma_j^2)]. \tag{5}$$

For detailed derivations of the reconstruction and KLD losses, see ref.⁴⁸. All details pertaining to the neural network architectures, training protocols, and hyperparameters are presented in Supplementary Table 1.

The generative capability of the VAE enables us to explore novel yet realistic truss structures, whose mechanical properties are immediately available at minimal computational cost through the property predictor \mathcal{F}_ω . With the joint property predictor as a regularizer, the generative modeling framework helps yield a deeper understanding of the latent space, which lacks physical interpretation and hence presents new opportunities for various downstream tasks by modifying the target of the structure-property predictor, e.g., towards the classification of deformation-mechanisms of truss lattices⁶¹, or the prediction of dispersion relations^{74,75} and the nonlinear response^{76,77}. Furthermore, our framework can be expanded to the simultaneous design of multiple properties by feeding the extracted features to a multi-task property predictor^{78–80}. By leveraging the correlations and shared information among different targets, we can effectively guide the design of truss lattices that have various desired properties by integrating the multi-task property predictor into a multi-objective optimization framework.

Performance of the VAE model

Our first goal is to correctly reconstruct truss structures: any given input lattice is mapped by the encoder into the latent space, from where the decoder reconstructs the truss lattice (Figure 2a). Defining the topology reconstruction accuracy as the percentage of correctly predicted links reveals that the trained VAE model accurately captures the topological features of trusses with an accuracy score of 99.9% for the adjacency matrix. The correlation plot between the true and reconstructed node positions is presented in Supplementary Fig. 4a. The model shows high quality in the reconstruction of the geometrical features, demonstrated by $R^2 \geq 99.9\%$ across the 3D components (x, y, z) of the node positions. A comparison of representative reconstructed truss structures and the corresponding original structures from the test dataset is shown in Supplementary Fig. 4b.

Next, we assess the performance of the surrogate model for predicting the 3D effective stiffness measures \mathbf{S} of trusses on an independent test set. As shown in the correlation plots between the true and predicted stiffness components in Supplementary Fig. 5, the trained model \mathcal{F}_ω overall achieves an $R^2 \geq 98.2\%$ accuracy across all stiffness components. Altogether, this confirms that our VAE model accurately reconstructs truss structures and predicts their effective stiffness properties.

With the jointly trained property predictor, the latent space is better organized in the sense that structures with similar mechanical properties are expected to cluster in the same region within the latent space (see also Supplementary Note 3.4.1), which gives important insight into the originally high-dimensional and intractable design space. Moreover, the property predictor works as an additional constraint, enforcing that points in the latent space

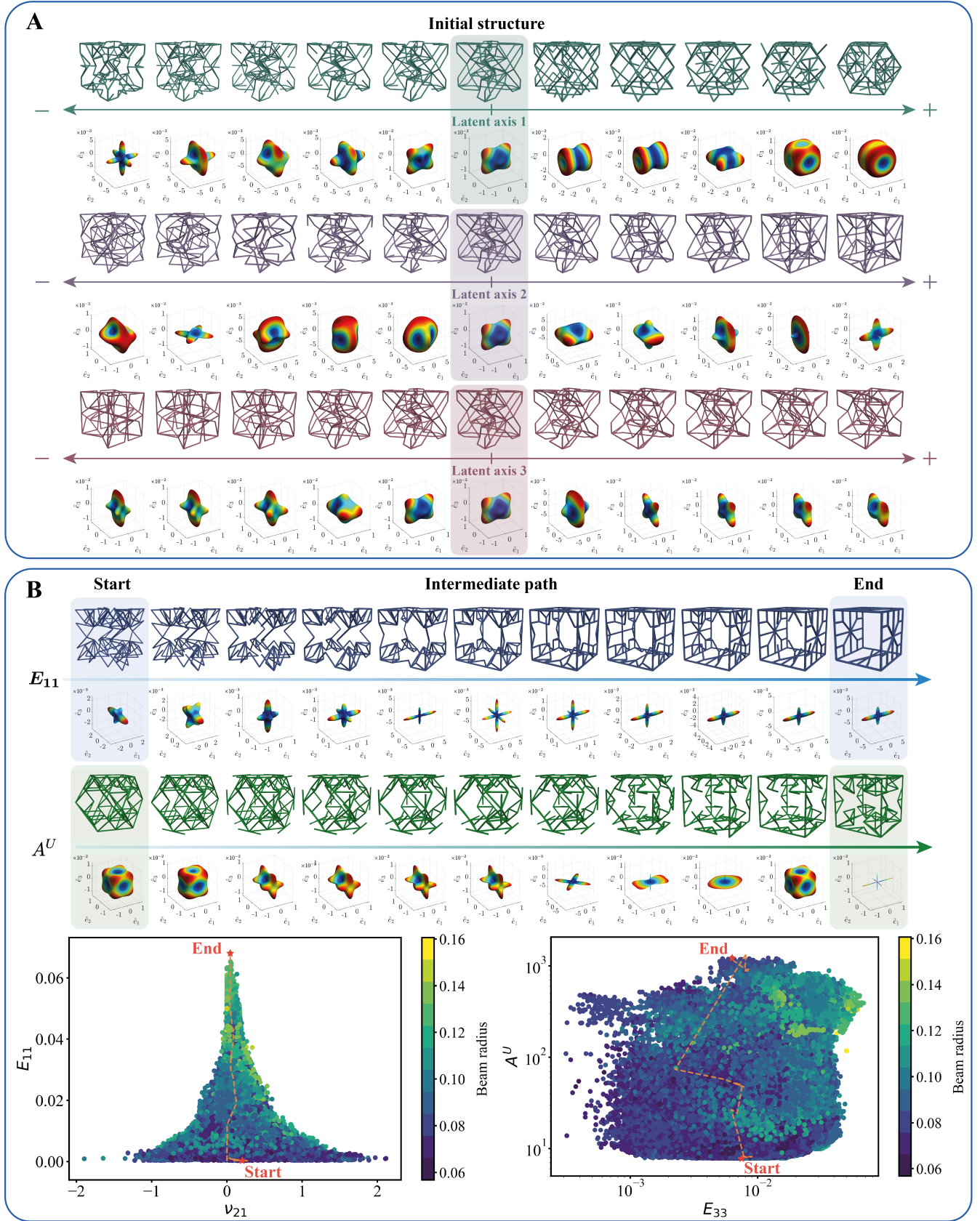


Figure 3. Representative examples of interpolation in the latent space. Samples are generated by (a) traversals along three different latent axes: (1) taken from the topology-specific, (2) shared topology and geometry, and (3) geometry-specific dimensions of the latent space; (b) interpolation between two points in latent space, whose corresponding trusses exhibit extreme mechanical properties (in terms of directional Young's modulus E_{11} and the universal anisotropy index A^U). Their corresponding 3D elastic surface evolution (obtained by FE homogenization) is shown along the interpolation path.

should decode into valid and realistic truss structures, thus preserving some mechanical property information while reducing the dimensionality. We evaluate the quality and efficiency of the latent space generation by randomly sampling 1,000 points from the latent space and using the decoder to reconstruct the corresponding structures. Results show that on average 82.3% (evaluated on 1,000 attempts of random sampling) of randomly-selected samples can be successfully decoded into valid (i.e., physically meaningful) truss topologies – we refer to this fraction as the *validity score*. While it is appealing to improve the quality of samples by imposing stronger regularization, such as increasing the weight of the KLD term in Equation (4) (also known as β -VAE⁸¹), the fidelity of the reconstruction will degrade due to the inherent trade-off between reconstruction accuracy and random sample quality in VAE models. In this work, we therefore adopt the annealing schedule for the weight of the KL-divergence term⁸² (details provided in Supplementary Note 3.1) to dynamically tune the importance given to the regularization and reconstruction losses, thus ensuring the flexibility of the VAE reconstruction.

Exploration in the latent space of truss lattices

The continuous and low-dimensional latent space with generalization ability is particularly advantageous for the design of new structures by traversing the latent space through simple arithmetic operations of the latent representation \mathbf{z} . While existing works that relied on a pixel/voxel-based parameterization have shown success in mapping the topology and mechanical properties in a latent space with a similar data-driven design framework²¹, they did not consider the impact of the different types of structural features (i.e., of connectivity and node positions) separately. In fact, manipulating the truss connectivity vs. moving nodes will expand the property space differently. For example, changes to the truss topology can have a strong effect on its deformation behavior (stretch- or bending-dominance depends primarily on the connectivity⁸³). To this end, we adopt the joint embedding model (details provided in Supplementary Note 3.2) to encode the topological and geometrical features in different dimensions of \mathbf{z} , while maintaining the total number of latent dimensions constant. A major advantage of this adjustment is that the importance given to each type of information can be adjusted by tuning the corresponding number of latent dimensions without increasing the model complexity. This provides flexibility and allows us to extract information that is only related to the topology or to the node position or to their interactions. As a consequence, traversals through the latent space along different axes give rise to significantly different changes in mechanical properties, which is enabled by the attributed latent embedding approach; i.e., each axis (each component of \mathbf{z}) stores specific information about the structural pattern transformation. Figure 3a shows an example of moving along three different latent axes (see also Supplementary Information Movies 1-3), which encode the information specifically for connectivity reconstruction, node positions reconstruction, or both – in each case starting from the same truss – which leads to the illustrated changes in structural topology, geometry, or both and the corresponding 3D stiffness (visualized as elastic surfaces).

While previous work has investigated the generation of new structures by moving along a path in latent space^{21,84}, it is usually intractable to obtain a disentangled representation of the original data space, since the complex correlation between entities is non-trivial to decompose. By contrast, our model uses a systematic latent representation for trusses, which admits human interpretation and where the truss connectivity and node positions can be independently altered. This is useful for many downstream tasks; e.g., for identifying the roles of different geometrical features and their impact on the effective truss performance.

As an illustration, we define an interpolation path between two points in latent space and reconstruct a continuous family of new trusses along the path with the decoder. The high validity score of our latent space ensures that the majority of generated new samples are physically feasible. (Possible issues such as a lack of connectivity or structural instability can be resolved by a light post-processing step.) For example, let us assume that two points in the high-dimensional latent space lie on the surface of a hypersphere rather than on a straight line, so we can interpolate between any two truss structures by applying the spherical linear interpolation⁸⁵ (slerp)

$$\text{SLERP}(\mathbf{z}_1, \mathbf{z}_2; \alpha) = \frac{\sin((1-\alpha)\theta)}{\sin\theta} \mathbf{z}_1 + \frac{\sin(\alpha\theta)}{\sin\theta} \mathbf{z}_2, \quad (6)$$

where \mathbf{z}_1 and \mathbf{z}_2 are the vectors of two points in the latent space, $\alpha \in [0, 1]$ is the interpolation parameter, and $\mathbf{z}_1 \cdot \mathbf{z}_2 = \cos\theta$. A detailed discussion on slerp and its comparison with linear interpolation is provided in Supplementary Note 3.4.2. Figure 3b presents two examples of interpolating between two truss structures that have significantly different mechanical behavior (e.g., structures with the largest and smallest Young’s modulus E_{11} , and with the largest and smallest universal anisotropy index A^U , which quantifies the degree of structural anisotropy⁸⁶ (details are provided in Supplementary Note 2)). Selected structures generated by the decoder along the interpolation path are visualized along with their respective elastic surfaces obtained from FE homogenization (see also Supplementary

Movie 4). Our smooth and continuous latent space ensures that, while the start- and end-point structures have opposite extremes of mechanical properties among the dataset, the transition of the structural geometries is smooth. This provides new opportunities for the design of continuous families of truss structures with property grading, which bypasses complex optimization algorithms operating in the high-dimensional, discrete design space. In the second example of Figure 3b (Supplementary Movie 5), we observed that – along the interpolation path between two points with extreme anisotropy values A^U – new structures are generated that have a considerably higher A^U -value than all trusses in the training dataset. This is possible, as we interpolate in the latent space instead of the property space. The jointly-trained property predictor encourages structures with similar mechanical performance to be located in the same region in latent space. Therefore, sampling in the vicinity of a point in latent space results in a rich family of trusses with similar properties (see also Supplementary Note 3.4.1). Moreover, new structures generated along a smooth interpolation path, or in the vicinity of the extreme values in the dataset, are expected to exhibit continuous property changes, including unprecedented extreme values.

Gradient-based optimization in the latent space

The continuous latent space successfully captures the underlying mechanical features of trusses rather than simply memorizing the training data. This enables the use of gradient-based optimization techniques to guide the tailoring of truss lattices to achieve desired properties and, furthermore, to extrapolate beyond the training domain. While the forward mapping from structure to property is straightforward, the inverse design problem is ill-posed due to the one-to-many mapping from the property space to the geometry space (i.e., multiple different truss candidates may lead to the same effective properties). This can be overcome by searching for a potential structure candidate, whose reconstructed stiffness matches the queried stiffness⁴⁴. To generate physically realistic truss structures or to obtain the sensitivities of properties with respect to structural features, we leverage automatic differentiation and use a backpropagation algorithm to obtain the gradients through the VAE model and the property predictor. Due to the discrete nature of truss topologies, unconstrained optimization in the latent space can be problematic and may result in invalid structures even with the variational term as a regularization, since there is no explicit constraint on the validity of generated samples when searching the whole latent space. As a remedy, we adopt an indirect approach by first reconstructing truss structures from their latent representation given by the optimizer, and passing them to the encoder to obtain the actual latent variables, which are then forwarded to the property predictor to predict the effective stiffness of generated structures (see Figure 2). The additional encoding-decoding process ensures that candidate structures proposed by the optimizer are valid.

To demonstrate the inverse design capabilities, we apply our generative modeling framework to design truss structures with extreme mechanical properties. Considering the one-to-many mapping of properties to structures and to have a reference, we first evaluate all structures in the training dataset towards the target property. Based on that data, initial guesses are chosen as the 100 closest matches in terms of the target property. Gradient-based optimizations for each initial guess are performed in parallel, and the best solution is identified by examining the FE-reconstructed properties of the 100 optimal solutions (the property predictor only serves as a computational shortcut to obtain the effective response during optimization). This approach identifies multiple candidate truss structures, which exhibit similar mechanical behavior – allowing for the selection of optimal structures under consideration of additional target attributes such as manufacturability or further properties of interest (see the detailed discussion in Supplementary Note 3.5).

Figure 4 illustrates three examples of the optimal design of truss lattices towards extreme properties. In all three cases, the trained generative models produce robust designs with properties far outside of the training domain through careful tuning of architectures, thus greatly expanding the limits of the property range. The first example maximizes the directional Young’s modulus E_{22} , for which Figure 4a shows the optimization path in the property space. Intermediate truss lattices are visualized to demonstrate the effect of the structural evolution (including the Voigt upper bounds $E_{\text{Voigt}} = E_s \cdot \rho$ and $G_{\text{Voigt}} = G_s \cdot \rho$). The optimization scheme gradually adjusts the beam arrangements along the e_2 -direction, exceeding the maximum Young’s modulus in the training dataset ($E_{22,\text{max}} = 0.068$) by 51.5%. The second example in Figure 4b shows structures optimized for a maximum auxetic behavior (i.e., for a maximum negative Poisson’s ratio ν_{21}) in the e_1 - e_2 -plane. The optimization scheme reaches an optimal structure with $\nu_{21} = -2.711$, which is a 42.9% improvement over the most negative Poisson’s ratio in the training set ($\nu_{21,\text{min}} = -1.897$). Finally, Figure 4c illustrates the search for near-pentamode structures⁸⁷, i.e., for fluid-like trusses with a high bulk-to-shear modulus ratio – being soft to shear but (close to) incompressible. The gradient optimization scheme here maximizes the ratio of the bulk modulus to the shear modulus. (Since the structures are anisotropic, we use the Voigt average bulk and shear moduli⁸⁸, K_V and G_V , respectively, for optimization.) Results show how the optimal structure yields a ratio of K_V/G_V that is 28.6% higher than the

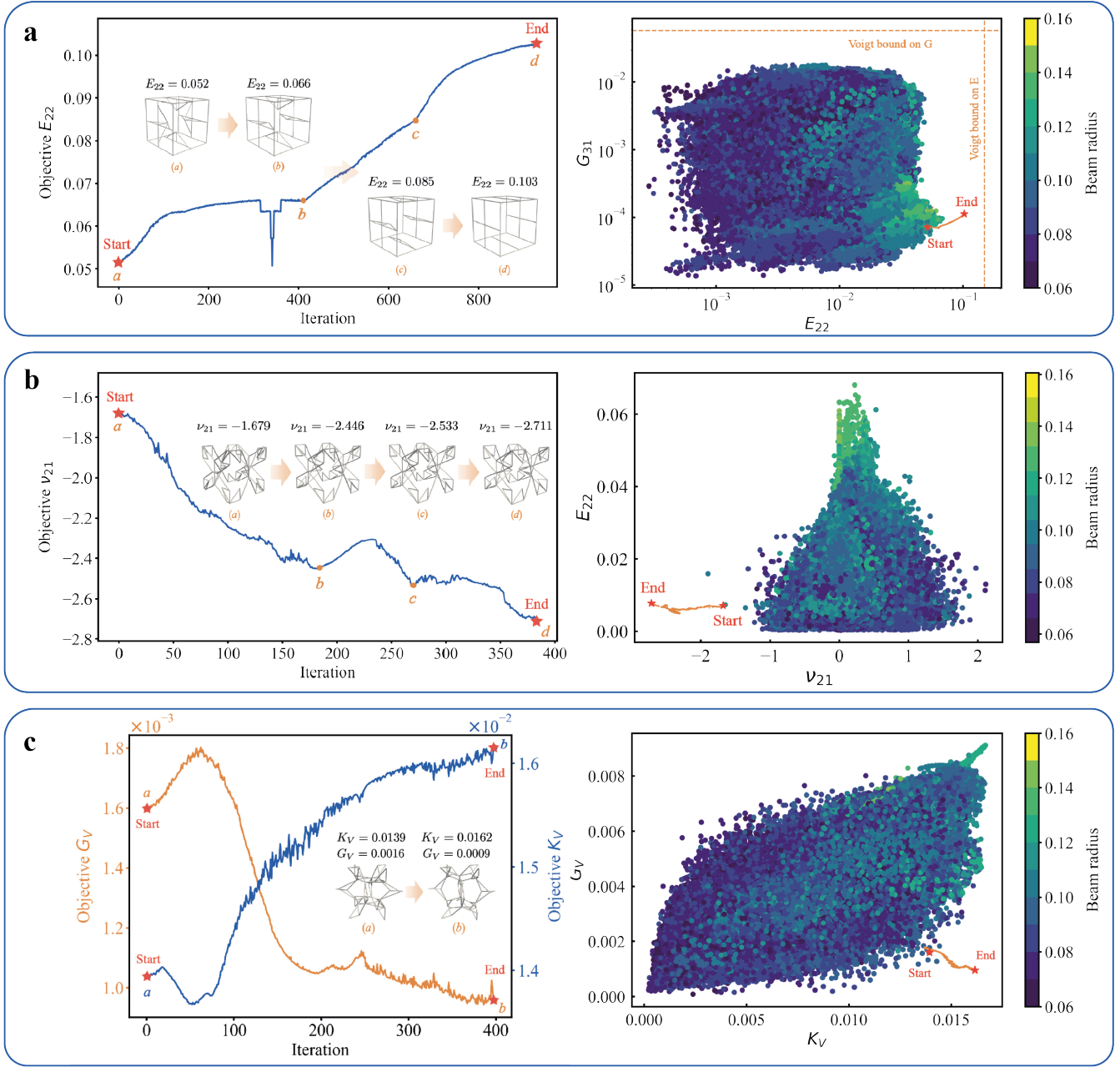


Figure 4. Inverse-designed truss metamaterials based on gradient optimization: (a) maximizing Young's modulus E_{22} , (b) minimizing Poisson's ratio ν_{21} , and (c) maximizing the bulk-to-shear-modulus ratio K_V/G_V of truss lattices. Each example shows the property evolution vs. the number of optimization iteration steps, including a few selected structures at the indicated points, as well as the property path compared to the training dataset in the relevant property spaces (each dot represents a truss in the training data, which is color-coded by the radius of the beams with circular cross-section).

maximum value contained in the training dataset (which is 14). While this may not be an impressive improvement compared to existing pentamode designs, we stress that – in all three optimization examples – the generative model improved the target properties significantly by only small structural modifications (compare, e.g., the initial and final structures in Figure 4, b and c). Such small changes, which are unlikely to be found by design intuition and experience, demonstrate the complexity of the design and property spaces and highlight the benefits of the presented approach.

Discussion

The presented generative modeling framework constructs a continuous, low-dimensional latent space of truss metamaterials. By analogy with molecules, we leverage the graph representation to interpret periodic trusses as graphs, thus providing an efficient, consistent, and general parameterization, which covers a wide range of truss structures and a tremendous space of anisotropic mechanical properties. Encoding the information related to the truss connectivity, the node positions, and their shared information in different dimensions of the latent representation enables a human interpretation of the otherwise intractable latent space. It also provides flexibility and tunability in manipulating structural features of truss lattices to achieve optimal properties. A major advantage of the unified and continuous latent representation is that novel truss structures can be conveniently generated by simple operations in the latent space, including sampling in the vicinity of known data points, traversing along the latent axes, and interpolating between two points. While classical VAEs often suffer from the issue of opacity and a lack of a physically meaningful representation, the proposed framework tackles this challenge by a jointly trained neural network to predict the truss properties from the latent space – thus allowing us to creatively navigate the latent space and to extrapolate with gradient-based optimization techniques to unseen, extreme properties outside the original training domain. This admits identifying optimal lightweight truss lattices with target combinations of, e.g., the elastic constants in 3D. The proposed design framework admits extension to other properties of truss metamaterials^{45,89,90} by modifying the property predictor as well as to other types of metamaterials^{37,44,91–94} by modifying the design parameterization. This highlights the potential of our framework to analyze and optimize a broad range of metamaterials. The physical interpretability and extrapolation ability open up new avenues for the discovery of new metamaterials and lend inspiration for designing cellular structures with tailored properties by tuning the architectural features.

Methods

Details of the dataset generation (Section 1), computational homogenization details (Section 2), the machine learning protocols (Section 3.1), the implementation of the overlapping embedding model (Section 3.2), the NN model performance (Section 3.3), exploration in the latent space including sampling (Section 3.4.1) and interpolation (Section 3.4.2), details on the gradient-based optimization in the latent space (Section 3.5), and the computational efficiency estimates (Section 3.6) are summarized in the Supplementary Information.

Data and code availability

The code used to train the generative modeling framework and obtain inverse designs of truss structures has been uploaded to Github (<https://github.com/li-zhengz/UnifyingTrussDesignSpace>). The corresponding training data has been deposited in the ETHZ Research Collection (<https://doi.org/10.3929/ethz-b-000618078>). The finite element code used for homogenization is contained in the *ae108* library and freely available from <http://ae108.ethz.ch/>.

Acknowledgements

The authors gratefully acknowledge the support from adidas and the discussions with Dr. Ladan Salari-Sharif and Derek Luther.

Funding: This research received financial support from adidas as well as from ETH Zurich through the ETH+ grant SynMatLab.

Authors contributions

Li Zheng: Methodology, Software, Validation, Data Curation, Visualization, Writing – Original Draft; **Sid Kumar:** Conceptualization, Methodology, Writing – Review & Editing, Supervision; **Dennis M. Kochmann:** Conceptualization, Methodology, Writing – Review & Editing, Supervision

Competing interests

The authors declare no competing interests.

References

1. Nicolaou, Z. G. & Motter, A. E. Mechanical metamaterials with negative compressibility transitions. *Nat. Mater.* **11**, 608–613 (2012).
2. Qu, J., Gerber, A., Mayer, F., Kadic, M. & Wegener, M. Experiments on metamaterials with negative effective static compressibility. *Phys. Rev. X* **7**, 041060 (2017).
3. Babaei, S. *et al.* 3D soft metamaterials with negative poisson's ratio. *Adv. Mater.* **25**, 5044–5049 (2013).
4. Yasuda, H. & Yang, J. Reentrant origami-based metamaterials with negative poisson's ratio and bistability. *Phys. Rev. Lett.* **114**, 185502 (2015).
5. Bückmann, T., Thiel, M., Kadic, M., Schittny, R. & Wegener, M. An elasto-mechanical unfeelability cloak made of pentamode metamaterials. *Nat. Commun.* **5**, 1–6 (2014).
6. Yuan, S., Chua, C. K. & Zhou, K. 3D-printed mechanical metamaterials with high energy absorption. *Adv. Mater. Technol.* **4**, 1800419 (2019).
7. Kumar, S., Ubaid, J., Abishera, R., Schiffer, A. & Deshpande, V. Tunable energy absorption characteristics of architected honeycombs enabled via additive manufacturing. *ACS Appl. Mater. & Interfaces* **11**, 42549–42560 (2019).
8. Guell Izard, A., Bauer, J., Crook, C., Turlo, V. & Valdevit, L. Ultrahigh energy absorption multifunctional spinodal nanoarchitectures. *Small* **15**, 1903834 (2019).
9. Chen, Y., Li, T., Scarpa, F. & Wang, L. Lattice metamaterials with mechanically tunable poisson's ratio for vibration control. *Phys. Rev. Appl.* **7**, 024012 (2017).
10. Li, Y., Baker, E., Reissman, T., Sun, C. & Liu, W. K. Design of mechanical metamaterials for simultaneous vibration isolation and energy harvesting. *Appl. Phys. Lett.* **111**, 251903 (2017).
11. Evans, A. G., Hutchinson, J. W. & Ashby, M. F. Multifunctionality of cellular metal systems. *Prog. Mater. Sci.* **43**, 171–221 (1998). Publisher: Elsevier.
12. Schaedler, T. A. *et al.* Ultralight metallic microlattices. *Science* **334**, 962–965 (2011).
13. Wallach, J. & Gibson, L. Mechanical behavior of a three-dimensional truss material. *Int. J. Solids Struct.* **38**, 7181–7196 (2001).
14. Deshpande, V. S., Fleck, N. A. & Ashby, M. F. Effective properties of the octet-truss lattice material. *J. Mech. Phys. Solids* **49**, 1747–1769 (2001).
15. Meza, L. R. *et al.* Reexamining the mechanical property space of three-dimensional lattice architectures. *Acta Materialia* **140**, 424–432 (2017).
16. Portela, C. M., Greer, J. R. & Kochmann, D. M. Impact of node geometry on the effective stiffness of non-slender three-dimensional truss lattice architectures. *Extrem. Mech. Lett.* **22**, 138–148 (2018).
17. Sharpe, C., Seepersad, C. C., Watts, S. & Tortorelli, D. Design of mechanical metamaterials via constrained bayesian optimization. In *International Design Engineering Technical Conferences and Computers and Information in Engineering Conference*, vol. 51753, V02AT03A029 (American Society of Mechanical Engineers, 2018).
18. Tran, A., Tran, M. & Wang, Y. Constrained mixed-integer gaussian mixture bayesian optimization and its applications in designing fractal and auxetic metamaterials. *Struct. Multidiscip. Optim.* **59**, 2131–2154 (2019).
19. Watts, S., Arrighi, W., Kudo, J., Tortorelli, D. A. & White, D. A. Simple, accurate surrogate models of the elastic response of three-dimensional open truss micro-architectures with applications to multiscale topology design. *Struct. Multidiscip. Optim.* **60**, 1887–1920 (2019).
20. Feng, J., Liu, B., Lin, Z. & Fu, J. Isotropic octet-truss lattice structure design and anisotropy control strategies for implant application. *Mater. & Des.* **203**, 109595 (2021).
21. Wang, L. *et al.* Deep generative modeling for mechanistic-based learning and design of metamaterial systems. *Comput. Methods Appl. Mech. Eng.* **372**, 113377 (2020).

22. Zheng, X. *et al.* Ultralight, ultrastiff mechanical metamaterials. *Science* **344**, 1373–1377 (2014).
23. Schumacher, C. *et al.* Microstructures to control elasticity in 3D printing. *ACM Transactions on Graph. (Tog)* **34**, 1–13 (2015).
24. Tancogne-Dejean, T. & Mohr, D. Elastically-isotropic truss lattice materials of reduced plastic anisotropy. *Int. J. Solids Struct.* **138**, 24–39 (2018).
25. Martínez, J. *et al.* Star-shaped metrics for mechanical metamaterial design. *ACM Transactions on Graph. (TOG)* **38**, 1–13 (2019).
26. Jia, Z., Liu, F., Jiang, X. & Wang, L. Engineering lattice metamaterials for extreme property, programmability, and multifunctionality. *J. Appl. Phys.* **127**, 150901 (2020).
27. Zhang, P. *et al.* Mechanical design and energy absorption of 3D novel hybrid lattice metamaterials. *Sci. China Technol. Sci.* **64**, 2220–2228 (2021).
28. Zhang, Z., Zhang, L., Song, B., Yao, Y. & Shi, Y. Bamboo-inspired, simulation-guided design and 3D printing of light-weight and high-strength mechanical metamaterials. *Appl. Mater. Today* **26**, 101268 (2022).
29. Xu, S., Shen, J., Zhou, S., Huang, X. & Xie, Y. M. Design of lattice structures with controlled anisotropy. *Mater. & Des.* **93**, 443–447 (2016).
30. Nguyen, J., Park, S.-i. & Rosen, D. Heuristic optimization method for cellular structure design of light weight components. *Int. J. Precis. Eng. Manuf.* **14**, 1071–1078 (2013).
31. Alzahrani, M., Choi, S.-K. & Rosen, D. W. Design of truss-like cellular structures using relative density mapping method. *Mater. & Des.* **85**, 349–360 (2015).
32. Chougrani, L., Pernot, J.-P., Véron, P. & Abed, S. Parts internal structure definition using non-uniform patterned lattice optimization for mass reduction in additive manufacturing. *Eng. with Comput.* **35**, 277–289 (2019).
33. Azizi, M., Aickelin, U., Khorshidi, H. A. & Shishehgharkhaneh, M. B. Shape and size optimization of truss structures by chaos game optimization considering frequency constraints. *J. Adv. Res.* **41**, 89–100 (2022).
34. Lumpe, T. S. & Stankovic, T. Exploring the property space of periodic cellular structures based on crystal networks. *Proc. Natl. Acad. Sci.* **118**, e2003504118 (2021).
35. White, D. A., Arrighi, W. J., Kudo, J. & Watts, S. E. Multiscale topology optimization using neural network surrogate models. *Comput. Methods Appl. Mech. Eng.* **346**, 1118–1135 (2019).
36. Mozaffar, M. *et al.* Deep learning predicts path-dependent plasticity. *Proc. Natl. Acad. Sci.* **116**, 26414–26420 (2019).
37. Vlassis, N. N., Ma, R. & Sun, W. Geometric deep learning for computational mechanics part i: anisotropic hyperelasticity. *Comput. Methods Appl. Mech. Eng.* **371**, 113299 (2020).
38. Wu, L., Zulueta, K., Major, Z., Arriaga, A. & Noels, L. Bayesian inference of non-linear multiscale model parameters accelerated by a deep neural network. *Comput. Methods Appl. Mech. Eng.* **360**, 112693 (2020).
39. Fuhg, J. N. *et al.* Model-data-driven constitutive responses: application to a multiscale computational framework. *Int. J. Eng. Sci.* **167**, 103522 (2021).
40. Zheng, L., Kumar, S. & Kochmann, D. M. Data-driven topology optimization of spinodoid metamaterials with seamlessly tunable anisotropy. *Comput. Methods Appl. Mech. Eng.* **383**, 113894 (2021).
41. Ma, W., Cheng, F., Xu, Y., Wen, Q. & Liu, Y. Probabilistic representation and inverse design of metamaterials based on a deep generative model with semi-supervised learning strategy. *Adv. Mater.* **31**, 1901111 (2019).
42. Chen, C.-T. & Gu, G. X. Generative deep neural networks for inverse materials design using backpropagation and active learning. *Adv. Sci.* **7**, 1902607 (2020).
43. Xue, T. *et al.* A data-driven computational scheme for the nonlinear mechanical properties of cellular mechanical metamaterials under large deformation. *Soft Matter* **16**, 7524–7534 (2020).

44. Kumar, S., Tan, S., Zheng, L. & Kochmann, D. M. Inverse-designed spinodoid metamaterials. *npj Comput. Mater.* **6**, 1–10 (2020).
45. Challapalli, A., Patel, D. & Li, G. Inverse machine learning framework for optimizing lightweight metamaterials. *Mater. & Des.* **208**, 109937 (2021).
46. Wang, Y., Zeng, Q., Wang, J., Li, Y. & Fang, D. Inverse design of shell-based mechanical metamaterial with customized loading curves based on machine learning and genetic algorithm. *Comput. Methods Appl. Mech. Eng.* **401**, 115571 (2022).
47. Bastek, J.-H., Kumar, S., Telgen, B., Glaesener, R. N. & Kochmann, D. M. Inverting the structure–property map of truss metamaterials by deep learning. *Proc. Natl. Acad. Sci.* **119**, e2111505119 (2022).
48. Kingma, D. P. & Welling, M. Auto-encoding variational bayes. *arXiv preprint arXiv:1312.6114* (2013).
49. Goodfellow, I. *et al.* Generative adversarial networks. *Commun. ACM* **63**, 139–144 (2020).
50. Sanchez-Lengeling, B. & Aspuru-Guzik, A. Inverse molecular design using machine learning: Generative models for matter engineering. *Science* **361**, 360–365 (2018).
51. Liu, Z., Zhu, D., Rodrigues, S. P., Lee, K.-T. & Cai, W. Generative model for the inverse design of metasurfaces. *Nano letters* **18**, 6570–6576 (2018).
52. Gurbuz, C. *et al.* Generative adversarial networks for the design of acoustic metamaterials. *The J. Acoust. Soc. Am.* **149**, 1162–1174 (2021).
53. Hamilton, W., Ying, Z. & Leskovec, J. Inductive representation learning on large graphs. *Adv. Neural Inf. Process. Syst.* **30** (2017).
54. Qiu, J. *et al.* Deepinf: Social influence prediction with deep learning. In *Proceedings of the 24th ACM SIGKDD international conference on knowledge discovery & data mining*, 2110–2119 (2018).
55. Zhang, M. & Chen, Y. Link prediction based on graph neural networks. *Adv. Neural Inf. Process. Syst.* **31** (2018).
56. Wu, Z. *et al.* Moleculenet: a benchmark for molecular machine learning. *Chem. Sci.* **9**, 513–530 (2018).
57. Jin, W., Barzilay, R. & Jaakkola, T. Junction tree variational autoencoder for molecular graph generation. In *International conference on machine learning*, 2323–2332 (PMLR, 2018).
58. Dai, M., Demirel, M. F., Liang, Y. & Hu, J.-M. Graph neural networks for an accurate and interpretable prediction of the properties of polycrystalline materials. *npj Comput. Mater.* **7**, 1–9 (2021).
59. Ross, E. & Hambleton, D. Using graph neural networks to approximate mechanical response on 3D lattice structures. *Proc. AAG2020-Advances Archit. Geom.* **24**, 466–485 (2021).
60. Meyer, P. P., Bonatti, C., Tancogne-Dejean, T. & Mohr, D. Graph-based metamaterials: Deep learning of structure-property relations. *Mater. & Des.* **223**, 111175 (2022).
61. Indurkar, P. P., Karlapati, S., Shaikhe, A. J. D. & Deshpande, V. S. Predicting deformation mechanisms in architected metamaterials using gnn. *arXiv preprint arXiv:2202.09427* (2022).
62. Panetta, J. *et al.* Elastic textures for additive fabrication. *ACM Transactions on Graph. (TOG)* **34** (2015).
63. Duvenaud, D. K. *et al.* Convolutional networks on graphs for learning molecular fingerprints. *Adv. Neural Inf. Process. Syst.* **28** (2015).
64. Simonovsky, M. & Komodakis, N. Graphvae: Towards generation of small graphs using variational autoencoders. In *International conference on artificial neural networks*, 412–422 (Springer, 2018).
65. You, J., Ying, R., Ren, X., Hamilton, W. & Leskovec, J. Graphrnn: Generating realistic graphs with deep auto-regressive models. In *International conference on machine learning*, 5708–5717 (PMLR, 2018).
66. Vlassis, N. N. & Sun, W. Geometric learning for computational mechanics part ii: Graph embedding for interpretable multiscale plasticity. *Comput. Methods Appl. Mech. Eng.* **404**, 115768 (2023).

67. Thomas, N. *et al.* Tensor field networks: Rotation-and translation-equivariant neural networks for 3D point clouds. *arXiv preprint arXiv:1802.08219* (2018).
68. Fuchs, F., Worrall, D., Fischer, V. & Welling, M. Se (3)-transformers: 3D roto-translation equivariant attention networks. *Adv. Neural Inf. Process. Syst.* **33**, 1970–1981 (2020).
69. Batzner, S. *et al.* E (3)-equivariant graph neural networks for data-efficient and accurate interatomic potentials. *Nat. communications* **13**, 2453 (2022).
70. Cai, C. *et al.* Equivariant geometric learning for digital rock physics: estimating formation factor and effective permeability tensors from morse graph. *Int. J. for Multiscale Comput. Eng.* **21** (2023).
71. Glaesener, R. N., Träff, E. A., Telgen, B., Canonica, R. M. & Kochmann, D. M. Continuum representation of nonlinear three-dimensional periodic truss networks by on-the-fly homogenization. *Int. J. Solids Struct.* **206**, 101–113 (2020).
72. Tishby, N., Pereira, F. C. & Bialek, W. The information bottleneck method. *arXiv preprint physics/0004057* (2000).
73. Leriche, S., Abitbol, J. L. & Karsai, M. Joint embedding of structure and features via graph convolutional networks. *Appl. Netw. Sci.* **5**, 1–24 (2020).
74. da Silva Ferreira, A., Malheiros-Silveira, G. N. & Hernández-Figueroa, H. E. Computing optical properties of photonic crystals by using multilayer perceptron and extreme learning machine. *J. Light. Technol.* **36**, 4066–4073 (2018).
75. Liu, C.-X. & Yu, G.-L. Predicting the dispersion relations of one-dimensional phononic crystals by neural networks. *Sci. Reports* **9**, 1–10 (2019).
76. Deng, B. *et al.* Inverse design of mechanical metamaterials with target nonlinear response via a neural accelerated evolution strategy. *Adv. Mater.* **34**, 2206238 (2022).
77. Maurizi, M., Gao, C. & Berto, F. Predicting stress, strain and deformation fields in materials and structures with graph neural networks. *Sci. Reports* **12**, 21834 (2022).
78. Capela, F., Nouchi, V., Van Deursen, R., Tetko, I. V. & Godin, G. Multitask learning on graph neural networks applied to molecular property predictions. *arXiv preprint arXiv:1910.13124* (2019).
79. Sanyal, S. *et al.* Mt-cgcnn: Integrating crystal graph convolutional neural network with multitask learning for material property prediction. *arXiv preprint arXiv:1811.05660* (2018).
80. Pasini, M. L., Zhang, P., Reeve, S. T. & Choi, J. Y. Multi-task graph neural networks for simultaneous prediction of global and atomic properties in ferromagnetic systems. *Mach. Learn. Sci. Technol.* **3**, 025007 (2022).
81. Higgins, I. *et al.* beta-vae: Learning basic visual concepts with a constrained variational framework. In *International Conference on Learning Representations* (2016).
82. Fu, H. *et al.* Cyclical annealing schedule: A simple approach to mitigating kl vanishing. *arXiv preprint arXiv:1903.10145* (2019).
83. Deshpande, V., Ashby, M. & Fleck, N. Foam topology: bending versus stretching dominated architectures. *Acta Materialia* **49**, 1035–1040, DOI: [https://doi.org/10.1016/S1359-6454\(00\)00379-7](https://doi.org/10.1016/S1359-6454(00)00379-7) (2001).
84. Gómez-Bombarelli, R. *et al.* Automatic chemical design using a data-driven continuous representation of molecules. *ACS Cent. Sci.* **4**, 268–276 (2018).
85. Shoemake, K. Animating rotation with quaternion curves. In *Proceedings of the 12th annual conference on Computer graphics and interactive techniques*, 245–254 (1985).
86. Ranganathan, S. I. & Ostoja-Starzewski, M. Universal elastic anisotropy index. *Phys. Rev. Lett.* **101**, 055504 (2008).
87. Milton, G. W. & Cherkaev, A. Which elasticity tensors are realizable. *J. Eng. Mater. Technol. The Asme* **117**, 483–493 (1995).
88. Voigt, W. *Lehrbuch der kristallphysik:(mit ausschluss der kristalloptik)*, vol. 34 (BG Teubner, 1910).

89. Wilt, J. K., Yang, C. & Gu, G. X. Accelerating auxetic metamaterial design with deep learning. *Adv. Eng. Mater.* **22**, 1901266 (2020).
90. Maurizi, M., Gao, C. & Berto, F. Inverse design of truss lattice materials with superior buckling resistance. *npj Comput. Mater.* **8**, 247 (2022).
91. Yamaguchi, K., Yasuda, H., Tsujikawa, K., Kunimine, T. & Yang, J. Graph-theoretic estimation of reconfigurability in origami-based metamaterials. *Mater. & Des.* **213**, 110343 (2022).
92. Kollmann, H. T., Abueidda, D. W., Koric, S., Guleryuz, E. & Sobh, N. A. Deep learning for topology optimization of 2d metamaterials. *Mater. & Des.* **196**, 109098 (2020).
93. Chen, Z., Ogren, A., Daraio, C., Brinson, L. C. & Rudin, C. How to see hidden patterns in metamaterials with interpretable machine learning. *Extrem. Mech. Lett.* **57**, 101895 (2022).
94. Alderete, N. A., Pathak, N. & Espinosa, H. D. Machine learning assisted design of shape-programmable 3D kirigami metamaterials. *npj Comput. Mater.* **8**, 191 (2022).

Unifying the design space of truss metamaterials by generative modeling

Li Zheng, Siddhant Kumar & Dennis M. Kochmann

Supplementary Information

1 Dataset generation

Supplementary Figure 1 shows the details of the generation of a diverse truss lattice dataset. We define the truss graph in the octant within a domain $\Omega_0 = [0, 1]^3 \subset \mathbb{R}^3$, which is populated into truss structures in the domain $\Omega = [-1, 1]^3 \subset \mathbb{R}^3$ through reflections about the three mutually orthogonal symmetry planes. We aim to construct a sufficiently large truss design space, which exploits the wide range of achievable material properties. Starting from the five elementary truss lattices shown in Step 1 of Supplementary Fig. 1, new structures are created by randomly perturbing both the node positions and connectivities for several iterations. Supplementary Figure 2 shows the node positions and connectivities of the five considered elementary truss structures. Node positions are altered by offsets defined in the natural coordinate system¹ and sampled from the uniform distribution $\lambda \sim \mathcal{U}(-0.5, 0.5)$. Based on the initial truss structures, new connectivities may be introduced by removing available nodes or inserting new nodes with the following constraints: (1) the established structure is a single connected component; (2) all beams are shorter than $r_{\max} = \sqrt{3}/2$ (times the unit side length of the unit cell); the maximum permissible length of a beam connection r_{\max} is chosen according to the longest connection in the initial five elementary trusses; (3) no dangling connections exist within the structure (every node has at least two connected beams). Each geometry is perturbed for 10 iterations to generate a library that contains a wide range of truss structures with several unique topologies. From the established set, we randomly sample two lattices with repetitions allowed, which are then superimposed according to their matching nodes to yield a more diverse dataset. The full dataset considered for training the generative models contains 965,736 lattices and their homogenized effective stiffness properties.

While we did not consider specific manufacturability constraints in this work, it is possible to enforce such constraints to narrow down the design space, depending on the requirements of specific applications. For instance, geometric constraints can be imposed to limit the maximum size or number of edges of the truss graph, while printability constraints¹ can be considered by ensuring that every node has at least one supporting node. Such considerations can easily be incorporated into our graph-based parameterization through conditions on the structure's geometry, utilizing the graph representation. Moreover, our framework can be extended to consider structural instability or failure, e.g., by integrating buckling strength² or compressive loading curves^{3,4} among the target properties towards the inverse design of buckling-resistant structures. Our generative modeling framework based on a graph representation of truss structures can be adapted to incorporate specific design considerations such as manufacturability requirements, making it a flexible framework that can be tailored to meet specific application goals. In addition, one advantage of our approach is that – when identifying an optimal structure – the latent space provides many structures with similar properties (nearby points in the latent space), so that secondary targets can also be implemented by choosing from a selection of potential trusses with different architectures yet similar effective stiffness.

2 Computational homogenization details

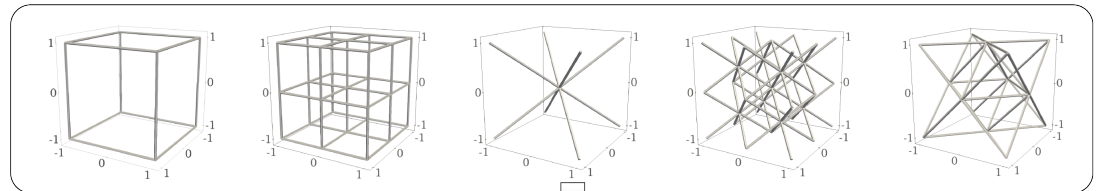
The effective stiffness tensor \mathbb{C} of all truss structures in our library are computed by finite element (FE) homogenization with periodic boundary conditions⁵, using on an in-house C++ FE code (available at <http://ae108.ethz.ch>). Each strut in the truss unit cell is modeled as a linear elastic Timoshenko beam with a circular cross-section. The strut radius of each unit cell is scaled to maintain a constant relative density of $\rho = 0.15$. We visualize the 3D anisotropic stiffness of truss lattices as elastic surfaces, which indicate the effective directional Young's modulus $E(\mathbf{d})$ for all directions $\mathbf{d} \in S^2$ as

$$E(\mathbf{d}) = \left(\sum_{i,j,k,l=1}^3 \mathbb{C}_{ijkl}^{-1} d_i d_j d_k d_l \right)^{-1}. \quad (1)$$

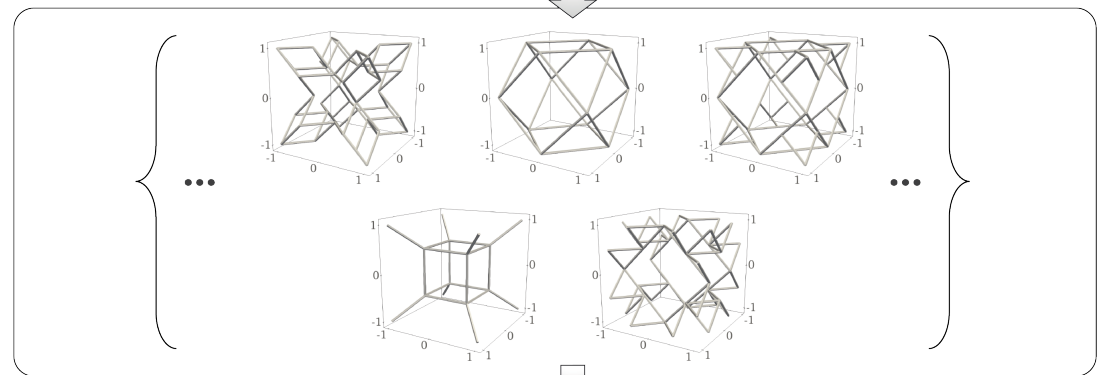
In the main article, we presented representative samples of novel truss lattices generated by interpolating between known structures that exhibit extreme universal anisotropy values A^U ⁶. A^U can be interpreted as a generalization of the Zener index⁷, which applies to structures with cubic symmetry and can be expressed as

$$A^U = 5 \frac{G_V}{G_R} + \frac{K_V}{K_R} - 6, \quad (2)$$

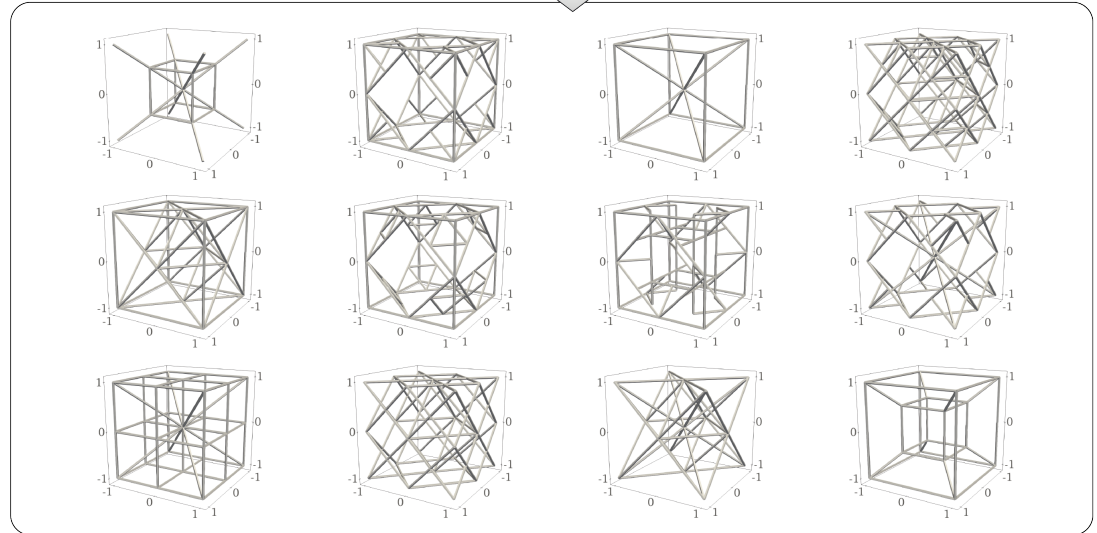
Step 1:
Initial topologies



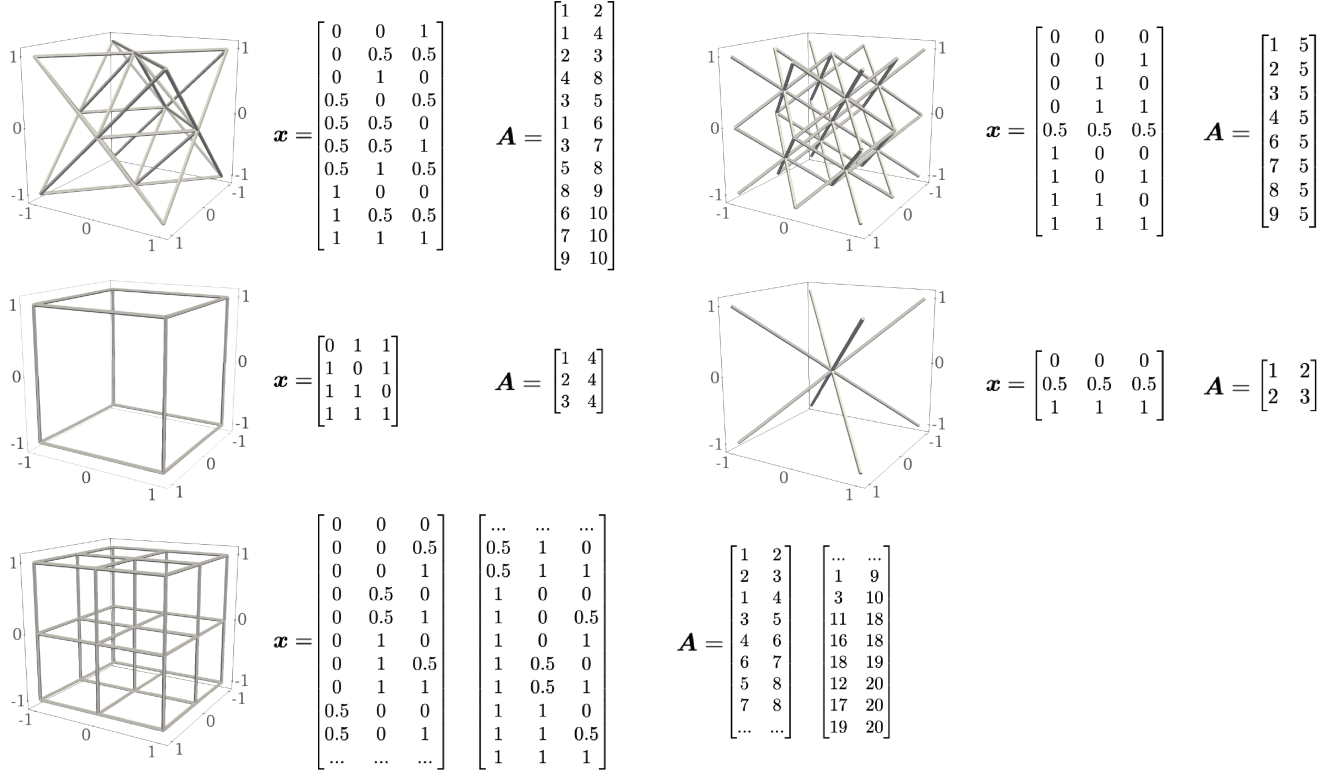
Step 2:
Connectivity
and node positions
exploration



Step 3:
Random sampling
and
superposition



Supplementary Figure 1. Overview of the truss dataset generation.



Supplementary Figure 2. Node positions \mathbf{x} and adjacency matrix \mathbf{A} of each of the five considered elementary truss unit cells.

where G_V and K_V are the Voigt estimates for, respectively, the shear and bulk moduli⁸, and G_R and K_R are the Reuss estimates for, respectively, the shear and bulk moduli⁹. Specifically, Reuss proposed the following relations for the bulk modulus K and shear modulus G in terms of the compliance components \mathbb{S}_{ijkl} :

$$K_R^{-1} = (\mathbb{S}_{1111} + \mathbb{S}_{2222} + \mathbb{S}_{3333}) + 2(\mathbb{S}_{1122} + \mathbb{S}_{1133} + \mathbb{S}_{2233}), \quad (3)$$

$$15G_R^{-1} = 4(\mathbb{S}_{1111} + \mathbb{S}_{2222} + \mathbb{S}_{3333}) - 4(\mathbb{S}_{1122} + \mathbb{S}_{1133} + \mathbb{S}_{2233}) + 3(\mathbb{S}_{4444} + \mathbb{S}_{5555} + \mathbb{S}_{6666}). \quad (4)$$

Analogously, we adopt the Voigt average bulk and shear moduli, calculated from the anisotropic stiffness components \mathbb{C}_{ijkl} as, respectively,

$$9K_V = (\mathbb{C}_{1111} + \mathbb{C}_{2222} + \mathbb{C}_{3333}) + 2(\mathbb{C}_{1122} + \mathbb{C}_{1133} + \mathbb{C}_{2233}), \quad (5)$$

$$15G_V = (\mathbb{C}_{1111} + \mathbb{C}_{2222} + \mathbb{C}_{3333}) - (\mathbb{C}_{1122} + \mathbb{C}_{1133} + \mathbb{C}_{2233}) + 3(\mathbb{C}_{4444} + \mathbb{C}_{5555} + \mathbb{C}_{6666}). \quad (6)$$

3 Machine learning framework

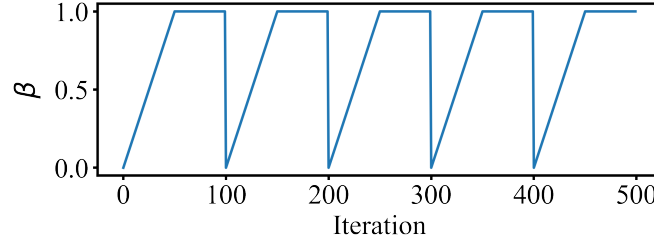
3.1 Protocols for NN training

Details of the optimized dimensions and hyperparameters (e.g., the number of hidden layers and nodes in each layer, activation functions, learning rates, etc) of the VAE model and the property predictor are provided in Supplementary Table 1. Thresholding is applied at the end of the connectivity decoder by a sigmoid function to achieve a binary connectivity matrix. 1% of the generated dataset is used for the tuning and optimization of hyperparameters. We used the PyTorch¹⁰ package throughout the implementation of the proposed generative learning framework and leveraged its automatic differentiation engine, autograd, to automatically obtain the gradients of the homogenized effective properties with respect to the structural and geometrical features towards the optimization and inverse design of truss lattices. Distinct from deterministic ML models, the training of the VAE model often involves a trade-off between the reconstruction accuracy and the model generative ability. For example, if the KL-divergence term is too small, the model completely ignores the latent representation and fails to learn an informative latent space (known as the KL-vanishing problem¹¹). To remedy this issue, we schedule the weight of the KL-divergence

	Encoder $\mathcal{Q}_\phi(G)$		Decoder $\mathcal{P}_\theta(G)$		Property predictor \mathcal{F}_ω
	Connectivity \mathbf{A}	Node positions \mathbf{x}	Connectivity \mathbf{A}	Node positions \mathbf{x}	
Input dimensions	278	27	$d_A(40)$	$d_x(40)$	$d(48) = d_A(40) + d_x(40) - d_{Ax}(32)$
Hidden dimensions	512, 512, 512, 128	640, 640, 640, 512	128, 512, 512, 512	256, 512, 640, 640	400, 800, 1000, 400, 400, 200
Output dimensions	$d(48) = d_A(40) + d_x(40) - d_{Ax}(32)$		278	27	9
Activation functions	ReLU		ReLU		ReLU
Optimization algorithm	Adam ¹⁴		Adam ¹⁴		Adam ¹⁴
Learning rate	5×10^{-4}		5×10^{-4}		5×10^{-4}
Batch size	512		512		512
Drop out	none		none		none

Supplementary Table 1. Dimensions and training hyperparameters of the optimized Variational Autoencoder and the property predictor models.

term β via the cyclical schedule¹² shown in Supplementary Fig. 3. The training process is split into several cycles, and in each cycle β is gradually increased from 0 to 1, using a linear function after 50 epochs. For a detailed performance comparison of various annealing schemes for β , see refs.^{11–13}.



Supplementary Figure 3. Annealing the KL-divergence term weight β with a cyclical schedule.

3.2 Overlapping embedding model

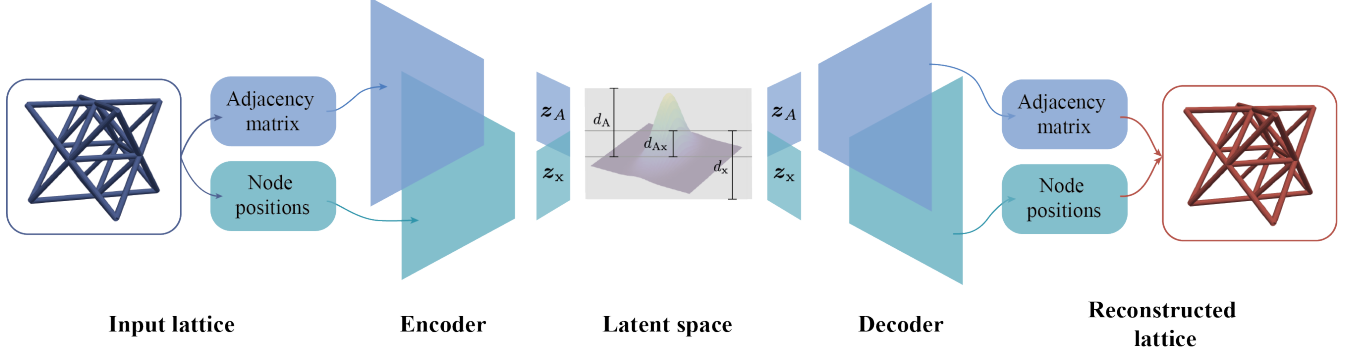
In order to accommodate the interdependencies between the structural topology (represented by the adjacency matrix) and node placements (represented by node features), we modify the VAE structure by restricting which part of a latent embedding is used for each task, as illustrated in Supplementary Fig. 4. Let $d_A - d_{Ax}$ be the number of latent dimensions allocated exclusively to topology, $d_x - d_{Ax}$ the number of dimensions exclusively allocated to geometry, and d_{Ax} the number of dimensions allocated to both. To keep the overall number of trainable parameters fixed, we reduce the outputs of the encoder ($\mu^A, \log \sigma^A \in \mathbb{R}^{d_A}$, and $\mu^x, \log \sigma^x \in \mathbb{R}^{d_x}$) to obtain the final latent representations $\mu, \log \sigma \in \mathbb{R}^d$ with $d = d_A + d_x - d_{Ax}$ as

$$\mu = \mu_{1:d_A-d_{Ax}}^A \oplus \frac{1}{2} (\mu_{d_A-d_{Ax}+1:d_A}^A + \mu_{1:d_{Ax}}^x) \oplus \mu_{d_{Ax}+1:d_x}^x, \quad (7)$$

$$\log \sigma = \log \sigma_{1:d_A-d_{Ax}}^A \oplus \frac{1}{2} (\log \sigma_{d_A-d_{Ax}+1:d_A}^A + \log \sigma_{1:d_{Ax}}^x) \oplus \log \sigma_{d_{Ax}+1:d_x}^x, \quad (8)$$

where \oplus denotes vector concatenation. Our rationale is that the topological and geometrical features of truss lattices are strongly correlated and, therefore, the overlapping dimensions should learn to extract the shared information between different entities, while preserving the topology-specific and geometry-specific information within their respective dimensions of latent representations. Compared to the non-overlapping model, where shared information is stored redundantly, the overlapping model, with its ability to capture joint information of different features, allows us to adjust the importance given to their interdependencies, while maintaining a constant number of training parameters. A comprehensive evaluation of the overlapping and non-overlapping models' performance across various tasks can be found in ref.¹⁵. The prediction accuracy of the model with different latent space dimensions is shown in Supplementary Table 2. We observe that increasing the shared dimensions allocated to both beyond a certain point does not significantly improve the model's performance. Therefore, we select the latent dimensions $d_A = 8$, $d_{Ax} = 32$, and $d_x = 8$, which strikes a reasonable balance between capturing essential features of truss structures and maintaining computational efficiency.

By decomposing different factors of variation while preserving the explicit interdependence between factors, the model captures the underlying relationships between these entities more effectively by exploiting the decomposed representations. This decomposition not only enhances the interpretability of the model¹⁶ but also improves its ability to extrapolate beyond the training distribution¹⁷. Overall, the above characteristics of the latent space make it a meaningful and structured representation of the original discrete design space, which is advantageous for the efficient optimization and generation of novel truss structures with targeted properties.



Supplementary Figure 4. Schematic of the overlapping embedding model. $d_A - d_{Ax}$ is the number of latent dimensions allocated exclusively to topology; $d_x - d_{Ax}$ is the number of dimensions allocated exclusively to geometry; d_{Ax} is the number of dimensions allocated to both.

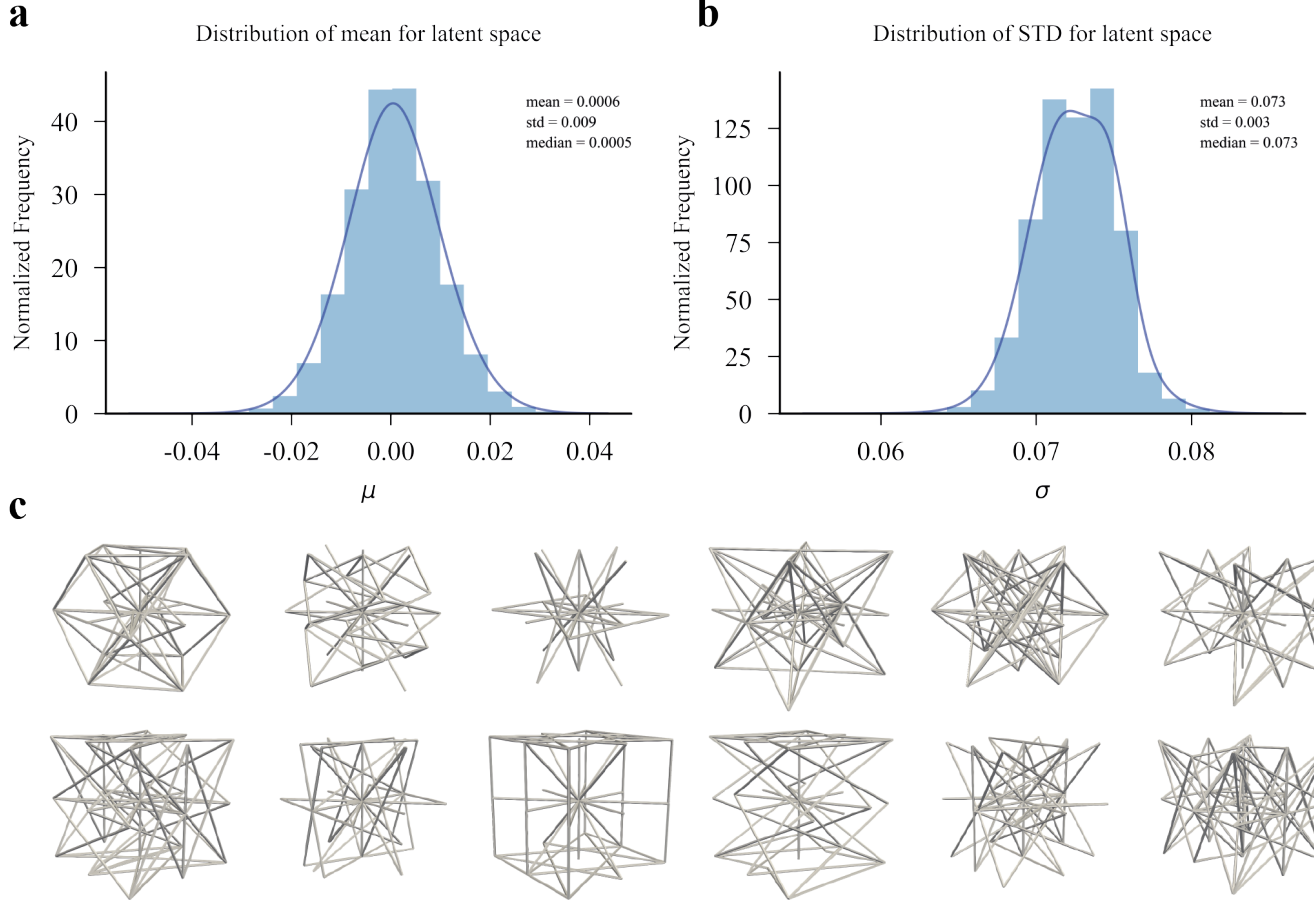
R^2 -scores for	A	(x, y, z)	C_{1111}	C_{1122}	C_{1133}	C_{2222}	C_{2233}	C_{3333}	C_{2323}	C_{3131}	C_{1212}
$d_A = 20, d_{Ax} = 8, d_x = 20$	0.990	0.995	0.985	0.957	0.974	0.976	0.967	0.982	0.970	0.974	0.968
$d_A = 16, d_{Ax} = 16, d_x = 16$	0.990	0.996	0.972	0.969	0.962	0.989	0.978	0.932	0.991	0.971	0.955
$d_A = 8, d_{Ax} = 32, d_x = 8$	0.999	0.999	0.995	0.987	0.989	0.995	0.990	0.995	0.983	0.983	0.982
$d_A = 4, d_{Ax} = 40, d_x = 4$	0.989	0.994	0.965	0.990	0.958	0.977	0.983	0.954	0.969	0.958	0.973

Supplementary Table 2. Comparison of the node positions reconstruction accuracy of the VAE model and the prediction accuracy of the property predictor using different latent dimension d_A, d_{Ax}, d_x . R^2 -scores are used as the primary metric.

3.3 NN model performance

Supplementary Figure 5a and b present the distribution and statistics of the mean and standard deviation of each dimension of the latent space. To illustrate the generative capacities of the VAE model, we randomly sampled latent vectors from the prior d -dimensional Gaussian distribution $z \sim \mathcal{N}(0, I)$, where $d = d_A + d_x - d_{Ax}$. The candidate latent vectors can then be decoded into novel truss structures beyond the training dataset, as shown in detail in Supplementary Fig. 5c. We evaluate the fidelity of the latent space by examining the percentage of randomly sampled points that can be decoded into valid truss structures satisfying the connectivity constraint (as described in Supplementary Note 1). Further, Supplementary Figure 6 lists the reconstruction accuracy of node positions along with representative examples of the reconstructed vs. true truss structures. Supplementary Figure 7 shows the prediction accuracy of all stiffness tensor components for the property predictor \mathcal{F}_w . The prediction accuracies are evaluated on a separate test dataset containing 2000 lattices and their corresponding homogenized stiffness tensor components.

In Supplementary Fig. 8 we further examine the two extreme outliers in Supplementary Fig. 6a-y by comparing the reconstructed vs. true structure and their corresponding elastic surfaces of the two outliers. We observe that, although there is a significant difference in the reconstructed vs. true node positions of structure (b) in Supplementary Fig. 8a, the difference in their effective structure and properties is minor. In addition, Supplementary Figure 6 shows that the reconstructed node positions correlate well with the ground truth with R^2 -values (≈ 0.999) close to unity for each component. Over 99.9% of all instances in the test data had errors within the interval $[-0.048, 0.048]$ for component $y \in [0, 1]$, indicating that the overall reconstruction performance is satisfactory. Therefore, we are confident that the VAE obtains a reliable estimation of the intrinsic underlying distribution and provides a sufficiently



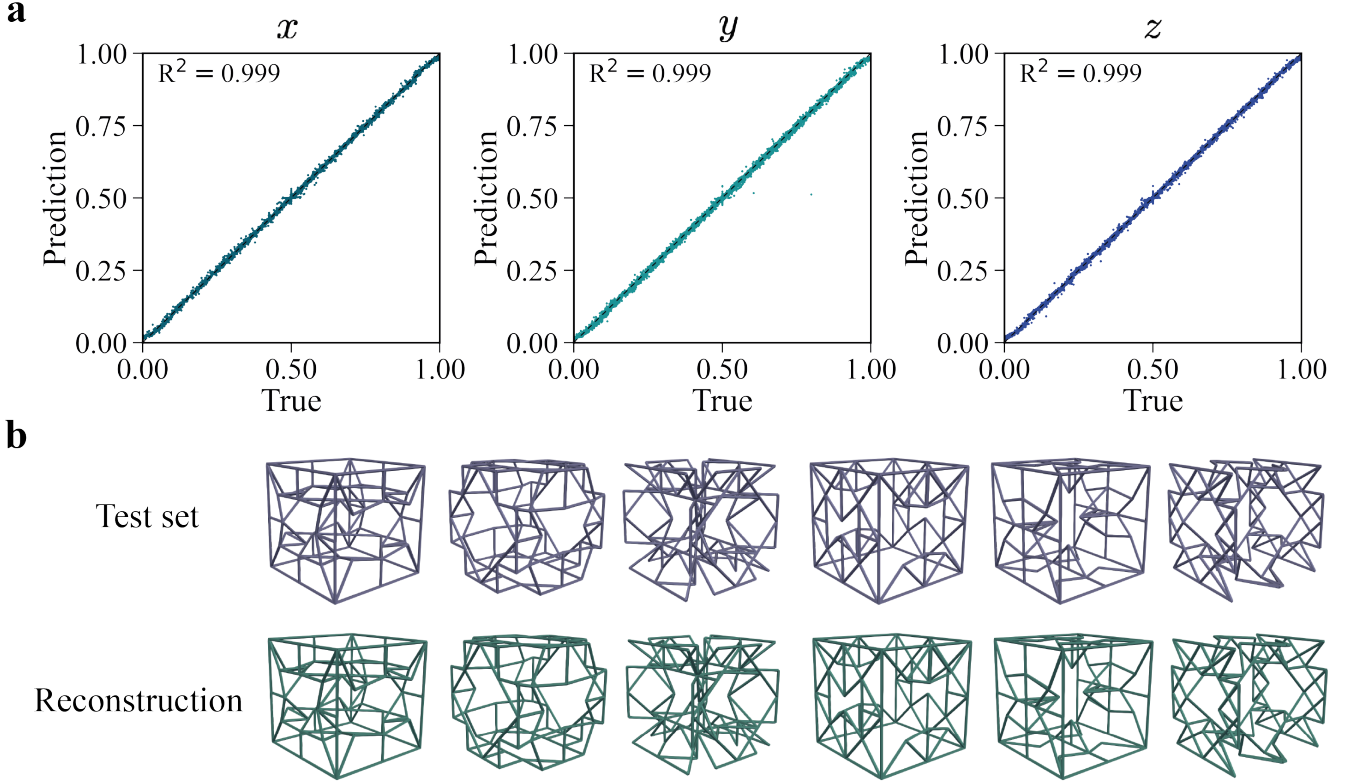
Supplementary Figure 5. Distribution and statistics of the latent space. (a) Distribution of the mean of the latent space coordinates. (b) Distribution of the standard deviation of the latent space coordinates. (c) Representative examples of truss structures generated by decoding from randomly-sampled points from the latent space.

good reconstruction of various truss structures.

Despite near-perfect overall accuracy, there are several potential reasons for the presence of extreme outliers in the correlation plots. One possible explanation is the trade-off between loss terms in this multi-task learning problem. Specifically, the VAE model is jointly trained with the property predictor as

$$\begin{aligned}
 \theta, \phi, \omega \leftarrow \arg \min_{\theta, \phi, \omega} & \underbrace{\frac{1}{N} \sum_{n=1}^N \left(\left\| \mathbf{A}^{(n)} - \mathbf{A}^{(n)'} \right\|^2 + \left\| \mathbf{x}^{(n)} - \mathbf{x}^{(n)'} \right\|^2 \right)}_{\text{reconstruction loss}} + \underbrace{\frac{1}{N} \sum_{n=1}^N \left\| \mathbf{S}^{(n)} - \mathcal{F}_{\omega}[\boldsymbol{\mu}^{(n)}] \right\|^2}_{\text{property prediction loss}} \\
 & + \underbrace{\sum_{n=1}^N D_{\text{KL}} \left(\mathcal{N} \left(\left[\mu_1^{(n)}, \dots, \mu_d^{(n)} \right]^{\top}, \text{diag} \left(\left[\sigma_1^{(n)2}, \dots, \sigma_d^{(n)2} \right]^{\top} \right) \right) \parallel \mathcal{N}(\mathbf{0}, \mathbf{I}) \right)}_{\text{Kullback-Leibler divergence}},
 \end{aligned} \tag{9}$$

where θ, ϕ, ω are model parameters of the VAE. Minimizing multiple loss functions simultaneously can be challenging because, e.g., the model capacity is limited or some loss terms are in conflict such as the inherent trade-off between the reconstruction robustness and generalization (given by the Kullback-Leibler divergence) in VAEs. A common strategy is to balance the losses as weighted sums of related terms during the multi-objective optimization, whereas the choice of weights will have a strong impact on the performance of the model on different tasks. In this work, we have compared the model performance with several selections of weights and selected the best model based on



Supplementary Figure 6. Evaluation of the reconstruction accuracy of the VAE model. (a)

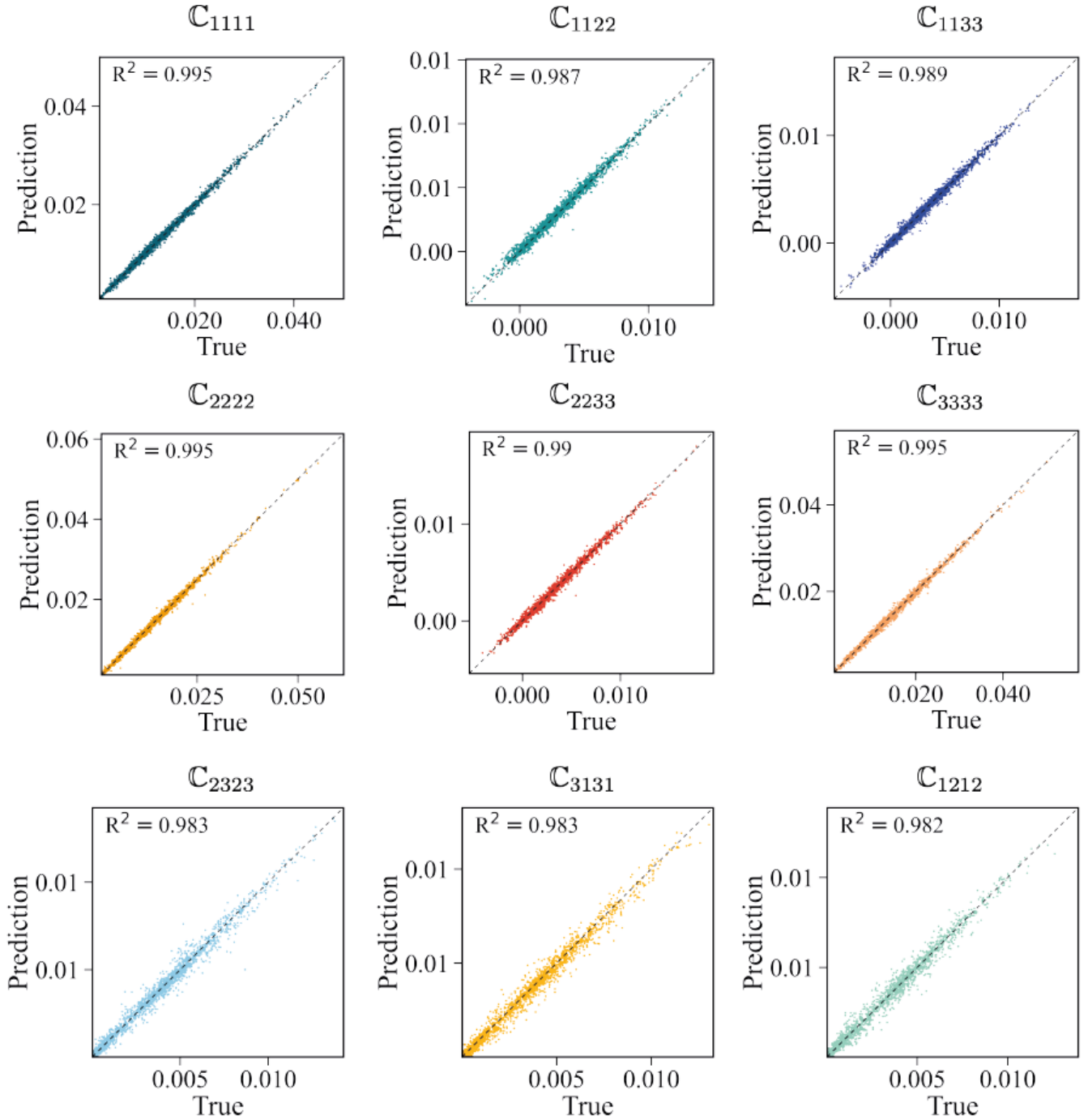
Reconstructed vs. true 3D components (x, y, z) of the node positions in the test dataset. The reconstructed node positions were computed using the decoder. Dashed lines represent the ideal lines with zero-intercept and unit-slope; the corresponding R^2 -scores are indicated. **(b)** Representative examples of reconstructed vs. true truss structures generated by the VAE model.

the property prediction accuracy, because our focus is the downstream task of optimizing truss lattices for target properties.

Alternatively, one can choose the best model according to other criteria depending on actual goals. For example, we modify Supplementary Equation 9 to include a weight $\lambda_{\text{recon}} > 0$ for the reconstruction loss as follows:

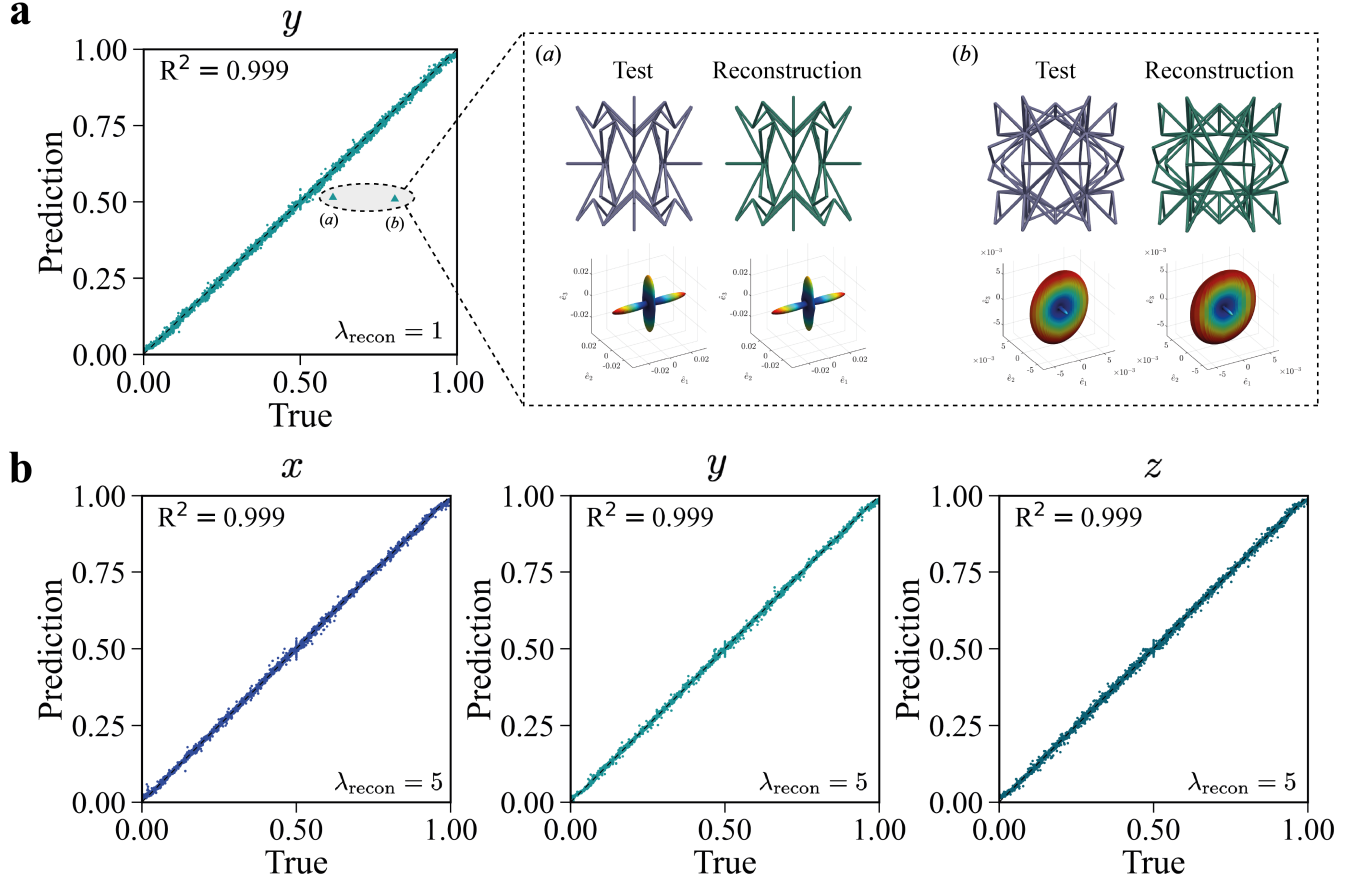
$$\begin{aligned}
 \theta, \phi, \omega \leftarrow \arg \min_{\theta, \phi, \omega} & \underbrace{\lambda_{\text{recon}} \frac{1}{N} \sum_{n=1}^N \left(\left\| \mathbf{A}^{(n)} - \mathbf{A}^{(n)'} \right\|^2 + \left\| \mathbf{x}^{(n)} - \mathbf{x}^{(n)'} \right\|^2 \right)}_{\text{reconstruction loss}} + \underbrace{\frac{1}{N} \sum_{n=1}^N \left\| \mathbf{S}^{(n)} - \mathcal{F}_{\omega}[\boldsymbol{\mu}^{(n)}] \right\|^2}_{\text{property prediction loss}} \\
 & + \underbrace{\sum_{n=1}^N D_{\text{KL}} \left(\mathcal{N} \left(\left[\mu_1^{(n)}, \dots, \mu_d^{(n)} \right]^{\top}, \text{diag} \left(\left[\sigma_1^{(n)2}, \dots, \sigma_d^{(n)2} \right]^{\top} \right) \right) \parallel \mathcal{N}(\mathbf{0}, \mathbf{I}) \right)}_{\text{Kullback-Leibler divergence}}.
 \end{aligned} \tag{10}$$

After training the model with a higher weight of the reconstruction loss term ($\lambda_{\text{recon}} = 5$, as opposed to $\lambda_{\text{recon}} = 1$ originally), Supplementary Figure 8b shows that the points are more centralized around the line with unit-slope and zero-intercept with fewer outliers in the correlation plots of reconstructed vs. true node positions (evaluated on the same test dataset used in the manuscript), which, however, can lead to a compromised or degraded property predictor accuracy due to the finite total capacity of the model, as shown in Supplementary Table 3.



Supplementary Figure 7. Evaluation of the prediction accuracy of the property predictor model.

Predicted vs. true components of the stiffness tensor \mathbb{C} in the test dataset. The predicted stiffness is computed using the property predictor \mathcal{F}_ω . All dashed lines represent the ideal line with zero-intercept and unit-slope; the corresponding R^2 -scores are indicated.



Supplementary Figure 8. Evaluation of the reconstruction accuracy of the VAE model. (a) Illustration of two selected extreme outliers from Supplementary Fig. 6a, showing the truss structures and their corresponding elastic surfaces. (b) Reconstructed vs. true 3D components (x, y, z) of the node positions in the test dataset using $\lambda_{\text{recon}} = 5$. Dashed lines represent the ideal lines with zero-intercept and unit-slope; the corresponding coefficient of determination R^2 -scores are indicated.

3.4 Exploration in the latent space

3.4.1 Sampling in the latent space

To illustrate that the VAE model tends to encode lattices with similar topologies and mechanical properties in the same region of the latent space, we randomly picked a starting point \mathbf{z}_0 in the latent space and sample points in its vicinity by adding Gaussian noise to the point, according to

$$\mathbf{z} = \mathbf{z}_0 + \beta \cdot \boldsymbol{\varepsilon}, \quad \text{with } \boldsymbol{\varepsilon} \sim \mathcal{N}(\mathbf{0}, \mathbf{I}), \quad (11)$$

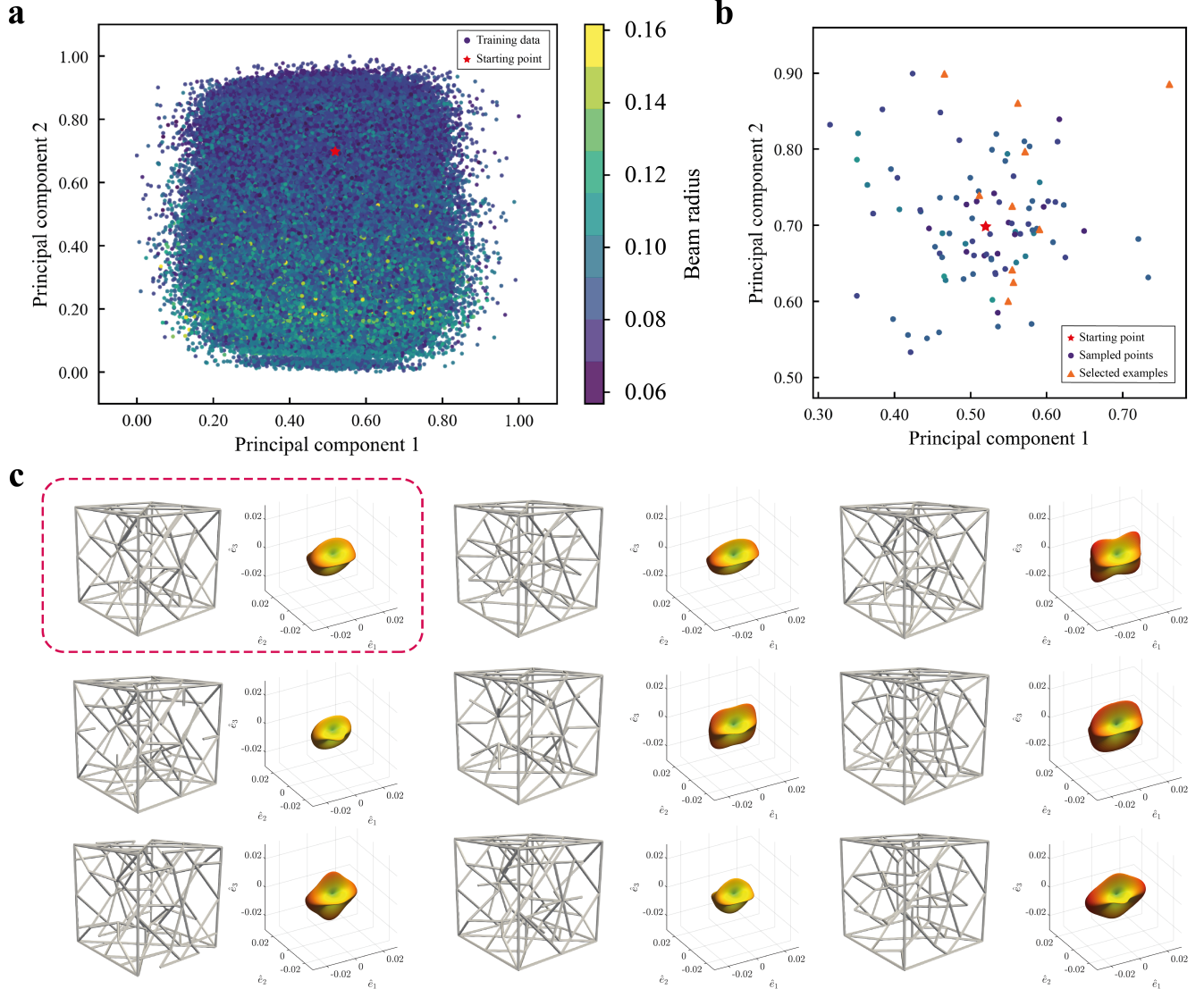
where $\beta \in [0, 1]$ is a scaling factor that determines the range of sampling. Supplementary Figure 9c shows representative examples of structures obtained by decoding the newly sampled points \mathbf{z} , along with their corresponding elastic surfaces computed by FEM homogenization. We observe that randomly sampled points in the neighborhood of the starting point exhibit similar topological features and mechanical properties. This similarity can be attributed to the property predictor that aims to learn the mapping from the latent space to properties. By incorporating physical knowledge into the VAE model, the predictor encourages the model to generate similar latent representations for trusses with similar properties for better prediction performance, as demonstrated in previous work with a VAE setup¹⁸ (albeit in a completely different context).

3.4.2 Interpolation in the latent space

Figure 3 of the main article shows representative examples of interpolation in the latent space. Specifically, the truss structures presented in Figure 3a were generated by traversals along different latent axes, which involves randomly selecting a truss structure, mapping it to the latent space to obtain its latent representation, and independently

R^2 -scores	x	y	z	\mathbb{C}_{1111}	\mathbb{C}_{1122}	\mathbb{C}_{1133}	\mathbb{C}_{2222}	\mathbb{C}_{2233}	\mathbb{C}_{3333}	\mathbb{C}_{2323}	\mathbb{C}_{3131}	\mathbb{C}_{1212}
$\lambda_{\text{recon}} = 1$	0.999	0.999	0.999	0.995	0.987	0.989	0.995	0.990	0.995	0.983	0.983	0.982
$\lambda_{\text{recon}} = 5$	0.999	0.999	0.999	0.982	0.961	0.966	0.981	0.965	0.979	0.980	0.981	0.976

Supplementary Table 3. Comparison of the node positions' reconstruction accuracy of the VAE model and the prediction accuracy of the property predictor, using $\lambda_{\text{recon}} = 1$ and $\lambda_{\text{recon}} = 5$.

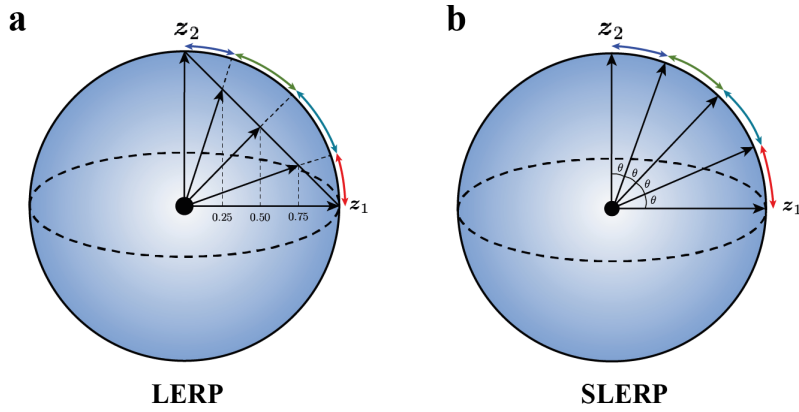


Supplementary Figure 9. Representations of sampling results in the latent space. (a) Two-dimensional PCA analysis of the latent space of the VAE model jointly trained with the property predictor. Colors indicate the beam radius of the truss structure. (b) Illustration of points sampled in the vicinity of the starting point ($\beta = 0.05$). (c) Representative examples of truss structures and their corresponding elastic surface generated by decoding from randomly-sampled points from the latent space. Highlighted in red in (a) and (b) is the starting point z_0 .

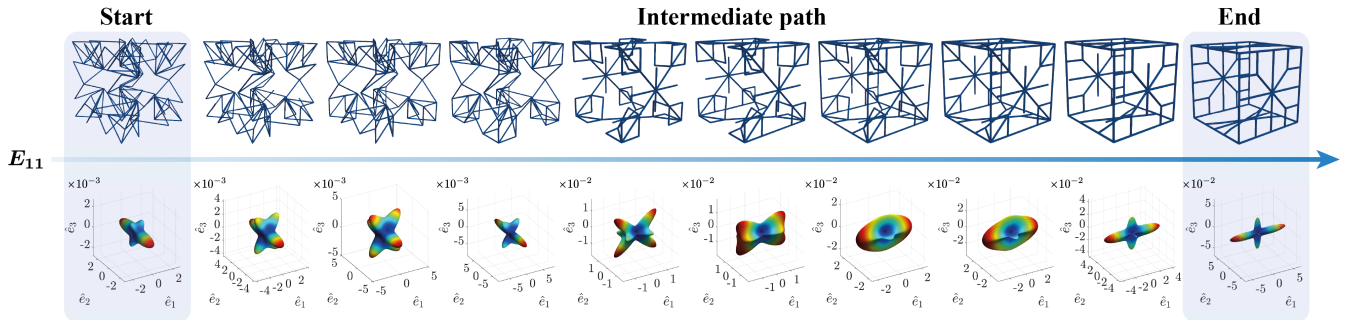
modifying each of the latent variables (corresponding to topology-specific, geometry-specific, and shared dimensions

in the latent space) along their negative and positive directions with a fixed step size. When interpolating between two points whose corresponding trusses exhibit extreme mechanical properties (as illustrated in Figure 3b of the manuscript), we employ *spherical linear* interpolation (slerp) rather than linear interpolation (lerp) in the latent space.

The choice of slerp over lerp is motivated by several factors. Constructing an approximately continuous latent space of truss structures provides a significant advantage, as the vector representation of truss lattices allows for the generation of novel structures by arithmetic operations. However, performing interpolation in a high-dimensional latent space with a Gaussian prior presents challenges. First, lerp assumes a straight line between points, which ignores the underlying structure of the data distribution, as schematically shown in Supplementary Fig. 10a below. Additionally, lerp measures the Euclidean distance between two points, which, however, does not necessarily indicate the similarity between truss structures in high-dimensional spaces. Consequently, the linearly interpolated points may jump or traverse regions of the latent space with similar representations, leading to inconsistent or unrealistic interpolations. In contrast, slerp takes into account the spherical structure of the latent space and follows the shortest arc on a hypersphere, which reduces artifacts or unnatural transitions between points. Supplementary Figure 11 shows that linear interpolation in our truss latent space produces less coherent geometries with abrupt changes in properties, whereas slerp interpolation (as shown in Figure 3b in the main article) exhibits smoother transitions in both geometries and properties along the interpolation path. The effectiveness of slerp has been demonstrated in the context of various generative models^{18,19} with uniform and Gaussian priors. Overall, slerp is generally more suitable for generating smooth and meaningful interpolations in the latent space of generative models.



Supplementary Figure 10. Illustration of the lerp and slerp interpolations with interpolation parameter $\alpha \in \{0.25, 0.5, 0.75\}$. (a) *Linear* interpolation: interpolated vectors are obtained by $\text{LERP}(z_1, z_2; \alpha) = \alpha \cdot z_1 + (1 - \alpha) \cdot z_2$. (b) *Spherical* interpolation: the interpolation is based on the angle between two points, and the resulting interpolation path follows a great circle on the hypersphere.

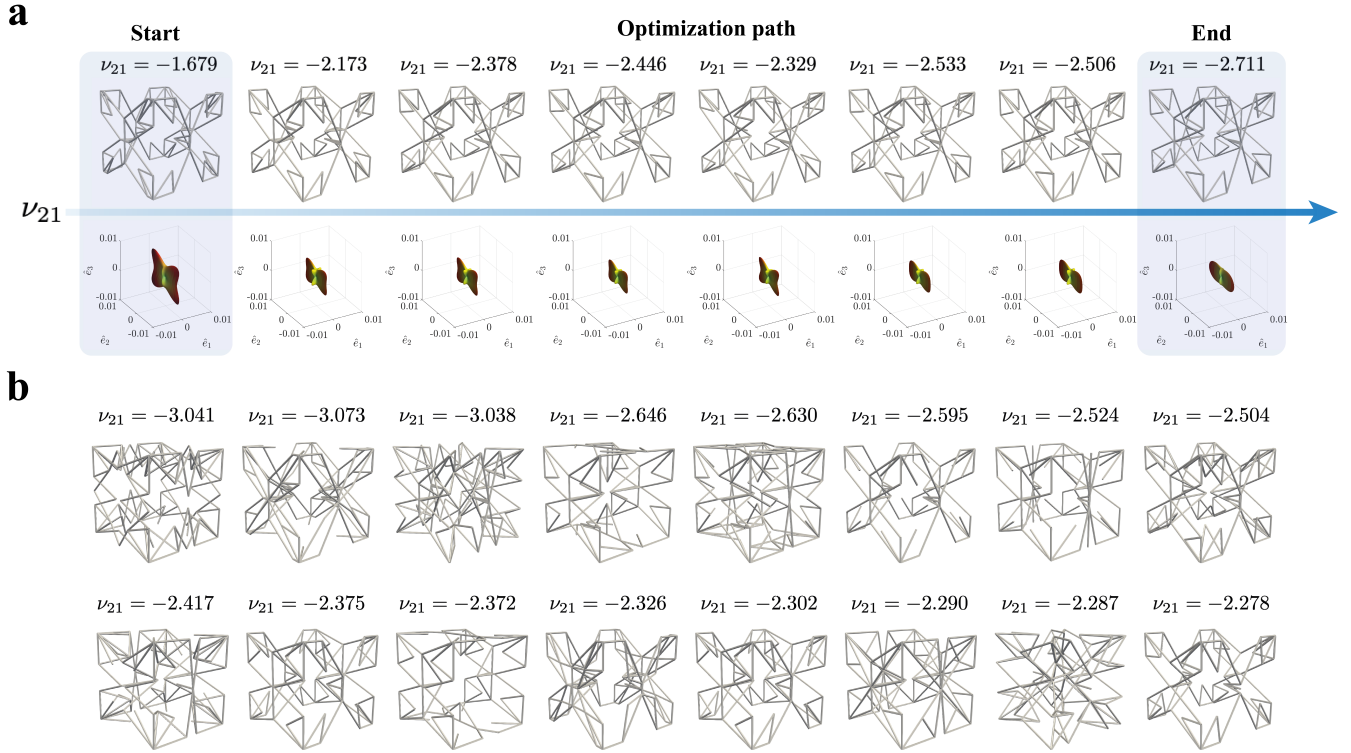


Supplementary Figure 11. Representative examples of linear (lerp) interpolation in the latent space. Samples are obtained by linear interpolation between two points in the latent space, whose corresponding trusses exhibit extreme directional Young's modulus E_{11} . Their corresponding 3D elastic surface evolution (obtained by FE homogenization) is shown along the interpolation path.

3.5 Gradient-based optimization in the latent space

For each optimization task, we first evaluate structures in the training dataset and select the 100 closest matches in terms of the target property as the initial guesses. Then, we perform gradient-based optimization for each initial guess in parallel and identify the optimal solution followed by FE homogenization-based validation of their properties. As a representative example, Supplementary Figure 12a illustrates truss structures obtained along the optimization path of minimizing Poisson's ratio ν_{21} (as shown in Figure 4b in the main article), which showcases the evolution of the geometries and properties.

To further emphasize that multiple similar truss structures can be generated, we have sampled in the neighborhood of the optimal solution based on Supplementary Equation 11. Supplementary Figure 12b shows that novel structures generated by sampling in the neighborhood of a point in the latent space exhibit similar topological features and mechanical properties (see also Supplementary Fig. 9). Notably, some structures generated through sampling in the latent space even display superior target properties compared with the solution we obtained through optimization, which highlights the potential of our generative framework in not only memorizing the training data but generalizing from a comprehensive truss dataset, effectively capturing the underlying mechanical relations. This finding further reinforces the notion that our generative framework is highly structured and is capable of leveraging the encoded mechanical property information within the latent space.



Supplementary Figure 12. Truss structures obtained from gradient optimization to minimize Poisson's ratio ν_{21} . (a) Evolution of truss geometries and their elastic stiffness properties along the optimization path. (b) Representative examples of truss structures obtained by sampling in the vicinity of the optimal solution in (a) with the sampling factor $\beta = 0.05$ using Supplementary Equation 11. The shown elastic stiffness surfaces were obtained by FE homogenization.

3.6 Computational efficiency estimates

To demonstrate the efficiency of our approach, Supplementary Table 4 presents an overview of the computational runtime, the software and hardware resources required for different tasks. Once trained offline, the property predictor can provide accurate stiffness predictions instantly. The computational time for stiffness calculation is significantly reduced compared to FEM homogenization, which provides a convenient shortcut for the optimal design of truss lattices.

Tasks	Software	Hardware	Runtimes
Dataset generation	Python	CPU (30 cores) [†]	4 hours
Stiffness computations (of the full dataset) using FEM	In-house C++ FEM code	CPU (30 cores) [†]	20 hours
Joint training of the VAE and property predictor \mathcal{F}_ω	PyTorch in Python	GPU [§]	4 hours
Stiffness prediction (of 2000 trusses) using \mathcal{F}_ω ¶	PyTorch in Python	GPU [§]	0.001 seconds
Optimal truss design using gradient-based optimization *	PyTorch in Python	CPU (30 cores) [†]	5 minutes

Supplementary Table 4. Overview of the computational runtime, the software and hardware resources required for different tasks. The reported runtimes are rough average estimates. [†]Computations were performed on the Euler IV cluster of ETH Zurich with two 18-core 2.7 GHz Intel Xeon Gold 6150 processors and 192 GB of DDR4 memory at 2666 MHz. [§]Computations were performed on a single Nvidia Quadro RTX 6000 24 GB GDDR6. ¶Runtimes for the property predictor are measured for one prediction on 2000 data samples. *Runtimes for optimization via the proposed ML framework are reported for parallel computation with 100 initial guesses (averaged over the different tasks shown in the main article).

References

1. Panetta, J. *et al.* Elastic textures for additive fabrication. *ACM Transactions on Graph. (TOG)* **34** (2015).
2. Maurizi, M., Gao, C. & Berto, F. Inverse design of truss lattice materials with superior buckling resistance. *npj Comput. Mater.* **8**, 247 (2022).
3. Wang, Y., Zeng, Q., Wang, J., Li, Y. & Fang, D. Inverse design of shell-based mechanical metamaterial with customized loading curves based on machine learning and genetic algorithm. *Comput. Methods Appl. Mech. Eng.* **401**, 115571 (2022).
4. Deng, B. *et al.* Inverse design of mechanical metamaterials with target nonlinear response via a neural accelerated evolution strategy. *Adv. Mater.* **34**, 2206238 (2022).
5. Glaesener, R. N., Träff, E. A., Telgen, B., Canonica, R. M. & Kochmann, D. M. Continuum representation of nonlinear three-dimensional periodic truss networks by on-the-fly homogenization. *Int. J. Solids Struct.* **206**, 101–113 (2020).
6. Ranganathan, S. I. & Ostoja-Starzewski, M. Universal elastic anisotropy index. *Phys. Rev. Lett.* **101**, 055504 (2008).
7. Zener, C. M. & Siegel, S. Elasticity and anelasticity of metals. *The J. Phys. Chem.* **53**, 1468–1468 (1949).
8. Voigt, W. *Lehrbuch der kristallphysik:(mit ausschluss der kristalloptik)*, vol. 34 (BG Teubner, 1910).
9. Reuß, A. Berechnung der fließgrenze von mischkristallen auf grund der plastizitätsbedingung für einkristalle. *ZAMM-Journal Appl. Math. Mech. für Angewandte Math. und Mech.* **9**, 49–58 (1929).
10. Paszke, A. *et al.* Pytorch: An imperative style, high-performance deep learning library. *Adv. Neural Inf. Process. Syst.* **32** (2019).
11. Bowman, S. R. *et al.* Generating sentences from a continuous space. *arXiv preprint arXiv:1511.06349* (2015).
12. Fu, H. *et al.* Cyclical annealing schedule: A simple approach to mitigating kl vanishing. *arXiv preprint arXiv:1903.10145* (2019).
13. Shao, H. *et al.* Controlvae: Controllable variational autoencoder. In *International Conference on Machine Learning*, 8655–8664 (PMLR, 2020).
14. Kingma, D. P. & Ba, J. Adam: A method for stochastic optimization. *arXiv preprint arXiv:1412.6980* (2014).
15. Leriche, S., Abitbol, J. L. & Karsai, M. Joint embedding of structure and features via graph convolutional networks. *Appl. Netw. Sci.* **5**, 1–24 (2020).
16. Lipton, Z. C. The mythos of model interpretability: In machine learning, the concept of interpretability is both important and slippery. *Queue* **16**, 31–57 (2018).

17. Montero, M. L., Ludwig, C. J., Costa, R. P., Malhotra, G. & Bowers, J. The role of disentanglement in generalisation. In *International Conference on Learning Representations* (2021).
18. Gómez-Bombarelli, R. *et al.* Automatic chemical design using a data-driven continuous representation of molecules. *ACS Cent. Sci.* **4**, 268–276 (2018).
19. White, T. Sampling generative networks. *arXiv preprint arXiv:1609.04468* (2016).